Bachelor's Thesis

Julius-Maximilians-
UNIVERSITÄT
WÜRZBURG

Institute of Computer Science
Satellite Communication and Radar Systems

Probing the Spiral Structure of the Milky Way Based on a Low-Cost Software-Defined Radio Approach

Angelika Ada Klär
2776278

Prof. Dr. Guido Dietl
Prof. Dr. Matthias Kadler
Supervisors

Submission
03.07.2025

License

Abstract

The 21 cm hydrogen line, first predicted by Ewen and Purcell in 1951, is a fundamental feature in radio astronomy, enabling the study of neutral hydrogen (HI) in the interstellar medium. Due to detected Doppler shifts of the HI clouds in our galaxy, calculations regarding galactic kinematics can reveal the spiral structure of the Milky Way. This thesis focuses on the detection and analysis of the hydrogen line using a Software-Defined Radio-based (SDR) receiver system. It outlines the theoretical background of the hydrogen line and its significance in astrophysical research, particularly in mapping the structure and rotational dynamics of the Milky Way's spiral arms.

Combined with the SDR, the observerational setup uses a commercial 2.4 GHz parabolic WiFi grid antenna, as well as a low-noise amplifier optimized for the hydrogen line. Data is collected every five degrees along the galactic plane with 2-minute integration time to improve the signal-to-noise ratio.

For signal processing, Fast Fourier Transform periodograms are utilized to analyze the spectral characteristics of the detected signals. Post-processing methods include polyphase filtering and noise reduction techniques to extract the hydrogen line peaks. Finally, the acquired data is used to derive the rotational curve of the Milky Way by calculating the Doppler shifts of the Hydrogen line clouds of our galaxy.

This study demonstrates the feasibility of conducting HI observations with accessible low-cost SDR-based instruments and highlights the challenges in weak signal detection, noise mitigation, and data interpretation in radio astronomy.

Contents

List of Figures

List of Tables

1 Introduction

1.1 Motivation

Radio astronomy has profoundly advanced our understanding of the universe by enabling observations of electromagnetic radiation in the radio wavelength domain, unhindered by dust and gas clouds that obscure visible light. A cornerstone discovery in this area is the detection of the 21 cm hydrogen line, first observed by Harold Ewen and Edward Purcell in 1951 [15]. This emission line originates from the hyperfine transition in neutral hydrogen atoms (HI), a quantum event detectable across interstellar and intergalactic distances due to the abundance of hydrogen in the cosmos. Observations of this line have been instrumental in unveiling the spiral structure of the Milky Way, measuring galactic rotation curves and probing the mass distribution within galaxies.

Neutral hydrogen pervades our galaxy, tracing its large-scale structure and kinematics. By measuring Doppler shifts in this emission line, astronomers determine the velocity distributions and dynamics of galactic gas clouds. Such measurements contribute directly to understanding phenomena including galaxy formation, dark matter distribution, and cosmic evolution. Furthermore, the 21 cm line acts as an observational probe unaffected by significant scattering or absorption, common issues with optical or infrared wavelengths, allowing clearer insights into galactic structures and dynamics.

1.2 Scope

This thesis presents an investigation into galactic hydrogen emission using a Software-Defined Radio (SDR)-based approach. The goal is to demonstrate that astrophysical research, traditionally requiring extensive resources, can be achieved using accessible hardware and advanced computational techniques. The project combines antenna design, hardware calibration, digital signal processing, and astrophysical data interpretation.

The primary scientific objective is to measure and analyze the Doppler-shifted hydrogen line emissions along the galactic plane, subsequently constructing a rotation curve and mapping the spatial distribution of neutral hydrogen clouds within the Milky Way. Furthermore, this thesis addresses questions regarding galactic morphology, kinematic modeling, and the feasibility of low-cost observational setups in astrophysical research.

1.3 Methodology

The experimental approach can be divided into four stages:

1.3.1 Hardware Setup and Calibration

A commercially available Wi-Fi grid dish antenna, originally tuned for 2.4 GHz is used. The feed is a dipole antenna, characterized both numerically via electromagnetic simulations and experimentally with a vector network analyzer (VNA). A theoretical tuning to the Hydrogen line's frequency of 1.42 GHz is described, though a practical execution has not been attempted.

1.3.2 Data Acquisition

An automated measurement system is established, which combines Python-based coordinate calculation scripts and an Arduino-driven rotor mechanism. This system sequentially points the antenna at predefined azimuth and elevation coordinates along the galactic plane, integrating incoming signals at each position for two minutes. The SDR hardware captures raw In-Phase (I) and Quadrature (Q) data for more flexibility in the subsequent digital analysis.

1.3.3 Digital Signal Processing (DSP)

The captured raw data undergoes a series of processing steps implemented in Julia, including filtering with a polyphase filterbank (PFB), spectral analysis via Fast Fourier Transform (FFT), and peak characterization using multi-Gaussian fitting. These processing techniques significantly enhance the detection sensitivity and accuracy of frequency estimation, necessary for reliable Doppler shift calculations.

1.3.4 Astrophysical Interpretation and Mapping

The frequency data, converted to radial velocities using relativistic Doppler equations, is used in the calculation of spatial positions for hydrogen clouds. By mapping these onto galactic coordinates, the resulting visualization provides insights into the spiral-arm structure and rotational dynamics of the Milky Way.

1.4 Relevance

The relevance of this project lies in demonstrating that fundamental astrophysical insights are accessible through modestly budgeted, highly integrated digital systems. In a broader context, it illustrates the democratization of scientific exploration in radio astronomy, lowering the barrier to participation for educational institutions and amateur scientists alike. Furthermore, detailed analyses of hydrogen distributions offer valuable data for ongoing astrophysical research, particularly concerning galactic evolution, dynamics, and the underlying dark matter distribution.

Since light pollution has continuously risen ever since the invention of the light-bulb, the night stars have disappeared from view, especially in urban areas. Researchers have since linked a low light pollution factor with a higher interest in astronomy amongst the population [2]. Solutions for light pollution are few, far and between, though shifting educational motivation into the radiowavelength domain with low-budget experiment setups, may help counteract this development.

This thesis thus contributes both methodologically and scientifically to explore innovative applications of software-defined radio technology and digital signal processing in modern astronomical research. Subsequent chapters systematically detail each stage of this project, from theoretical foundations and antenna simulations through to data acquisition, processing, and astrophysical interpretation.

2 The Hydrogen Line

The 21 cm line with a rest frequency of $f_0 = 1420.405\,\text{MHz}$ [23] is one of the cornerstones of modern radio astronomy. It stems from the hyperfine splitting of the ground state of atomic hydrogen, as depicted in Fig. 2.1, which is the most abundant element in the universe. Observations of the 21 cm line play a central role in understanding galactic structure, dynamics, and large-scale evolution, because neutral hydrogen is widely distributed within galaxies.

2.1 Historical Context

Although the theoretical groundwork for the hyperfine transition was largely established by Dutch astronomer H. C. van de Hulst in the 1940s, it was Harold Ewen and Edward Purcell who first confirmed the 21 cm line experimentally in 1951 [15]. This observation demonstrated that galactic neutral hydrogen could be detected and systematically mapped using radio telescopes, opening a new window onto the structure and evolution of the Milky Way.

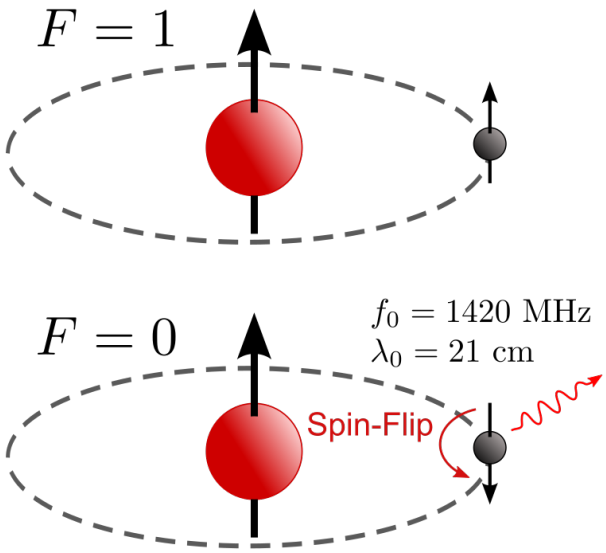

Figure 2.1: Illustration of the Hydrogen Spin-Flip [25]

2.2 Hyperfine Splitting and Spin-Flip Transition

Each hydrogen atom consists of a single electron bound to a proton.[1] Both electrons and protons, have spin angular moments that are oriented either parallel or anti-parallel to one another. These two configurations lead to slightly different energy levels, known as hyperfine splitting, as depicted in 2.1. The energy difference between the parallel (higher-energy) and anti-parallel (lower-energy) configurations is extremely small, it corresponds to the emission of a photon at 21 cm wavelength.

Formally, the transition is often called *forbidden*, as it violates the quantum mechanical selection rules for a electric dipole transition. Still, the transition can occur with a very small radiative transition rate of $2.9 \times 10^{-15}\,\mathrm{s}^{-1}$ [47] corresponding to a radiative lifetime of the excited state of about 11 million years.

Across the immense populations of neutral hydrogen atoms in the Interstellar Medium (ISM), a sufficiently large number of these rare events occurs in a more collision-free environment to produce a measurable radio signal. In denser or hotter environments, collisions and other deexcitation mechanisms can dominate, suppressing the spin-flip emission. In contrast, under typical ISM conditions, where densities are on the order of one atom per cubic centimeter and temperatures range from tens to hundreds of Kelvin, collision rates are low enough that spin-flip emission remains a significant process. Moreover, the abundance of hydrogen, about 75% by mass in most regions of the universe, ensures that, even with a low per-atom emission probability, the cumulative signal becomes observable.

2.3 Observational Significance

From an observational standpoint, the 21 cm line is particularly valuable as the signal is minimally absorbed by dust or gas, allowing the line to be observed across great distances and through obscured regions of the galaxy. This allows for small Doppler shifts of the 21 cm line to be detectable and to provide a direct measure of gas velocity along the line of sight. By mapping these velocity structures, the rotation curves of galaxies can be determined, large-scale spiral arm organization can be studied and the mass distribution within the galactic disk can be estimated. Furthermore, neutral hydrogen exists in large reservoirs not only within galaxies but also in intergalactic filaments. This makes the 21 cm line a powerful tool for tracing the overall distribution of matter on multiple scales.

Because the 21 cm line probes the distribution and motion of hydrogen, it is integral to understanding the spiral structure of galaxies and their dark matter content. Velocity measurements along different lines of sight reveal the characteristic rotation curve, which often exhibits a flat or slowly rising profile at large galactocentric radii. Such measurements provide key evidence for the presence of dark matter and refine models of galactic mass distributions.

In this work, a mapping of the spiral arms of the Milky Way is performed. The Doppler

[1] The neutron-containing hydrogen isotopes Deuterium and Tritium do not contribute to the 21cm line due to their different nuclear spin and magnetic moment.

shift of the 21cm line enables a measurement of the velocity of hydrogen gas relative to Earth. With this information, the rotational curves of the Milky Way can be calculated and the spiral arms mapped.

3 Simulation of the Dipole

This chapter presents the theoretical background and numerical simulation results for a half-wave dipole antenna intended to operate at the hydrogen line frequency of 1.42 GHz. Commercial WiFi grid-dish feeds designed for 2.4 GHz were modelled in EZNEC Pro/2+ [29] and theoretically adapted by extending the dipole arms. Due to time constraints, an execution of this theoretical work was not possible.

Numerical models were simulated using thin wire segments in free space. The dipole element radius was set to 1 mm, segmented into 41 equal sections, and center-fed with a 50 GHz source. Frequency sweeps covered 1.0 GHz to 3.0 GHz for wideband behaviour and finer sweeps around 1.42 GHz to resolve the primary resonance. No ground plane or reflector was included.

3.1 Dipole Antenna Theory

The half-wave dipole is widely used due to its natural resonant property at its operating frequency. The length L of a resonant half-wave dipole antenna is approximately given by:

$$L \approx n\,\frac{\lambda}{2}, \quad n = 1, 3, 5, \ldots \tag{3.1}$$

Here $\lambda = c/f$ is the free-space wavelength with $c \approx 3 \times 10^8\,\mathrm{m\,s^{-1}}$ and f as the frequency. At this length, the antenna exhibits standing wave patterns with current maxima at its center and voltage maxima at its endpoints. A half-wave ($n = 1$) dipole therefore has

$$L_{\lambda/2} \approx \frac{c}{2f}\,. \tag{3.2}$$

In free space a perfectly thin half-wave dipole exhibits a radiation resistance of about 73 Ω and an SWR of approximately 1.5:1 when driven by a 50 Ω line.

3.2 Real-life conditions

The simulations assume an ideal thin-wire dipole in free space without any supporting hardware, balun, or reflector. In practice, dielectric supports, coaxial feedlines and proximity to metal structures will perturb the resonant frequency and input impedance. End-effects due to finite wire diameter and insulation further shift resonance, necessitating trimming of the element length by approximately $5 - 10\%$. The feedpoint impedance will also depart from the ideal 73 Ω, requiring matching techniques if optimal SWR is desired [1].

3.3 SWR Simulations

3.3.1 2.4 GHz Design

A half-wave dipole sized for 2.4 GHz was simulated according to the ideal half-wave dipole in real conditions. Figure 3.1 shows an SWR minimum of 1.42:1 at approximately 2.2 GHz. This detuning can mainly be attributed to end-effect capacitive loading in a real dipole element when the length is not adjusted.

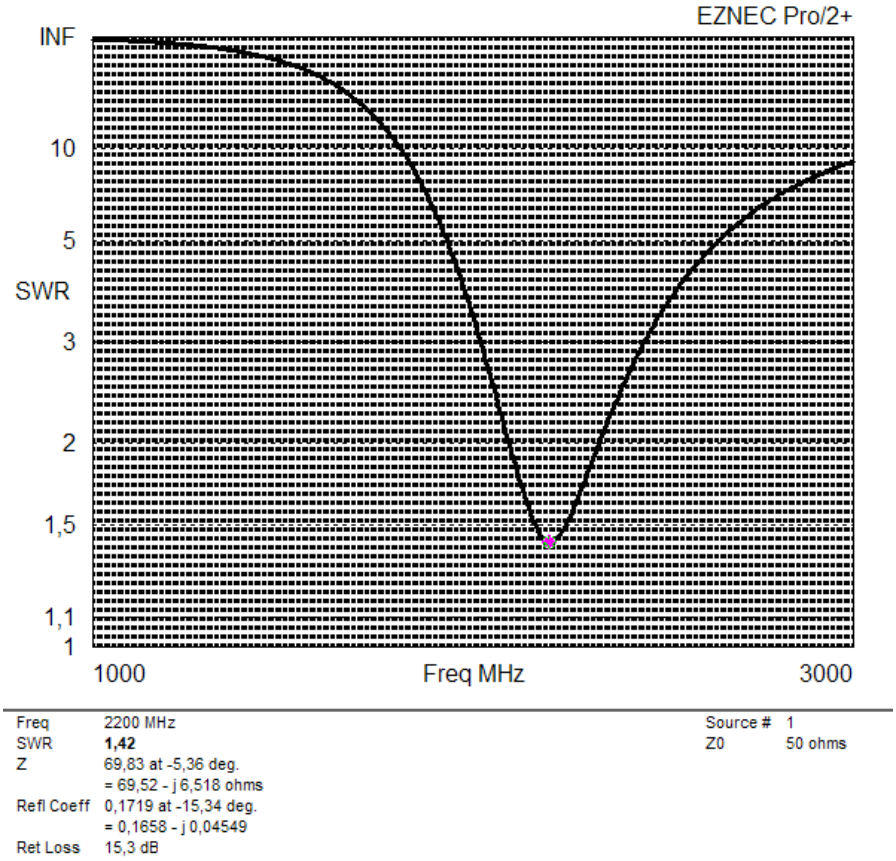

Figure 3.1: Simulated SWR of an ideal half-wave dipole at 2.2 GHz in free space.

3.3.2 Resonance at 1.42 GHz

The simulated SWR sweep of the dipole for 1.42 GHz that is 10% shorter than the ideal half-wavelength dipole, is shown in Fig. 3.2. A minimum SWR of 1.30:1 occurs at that frequency.

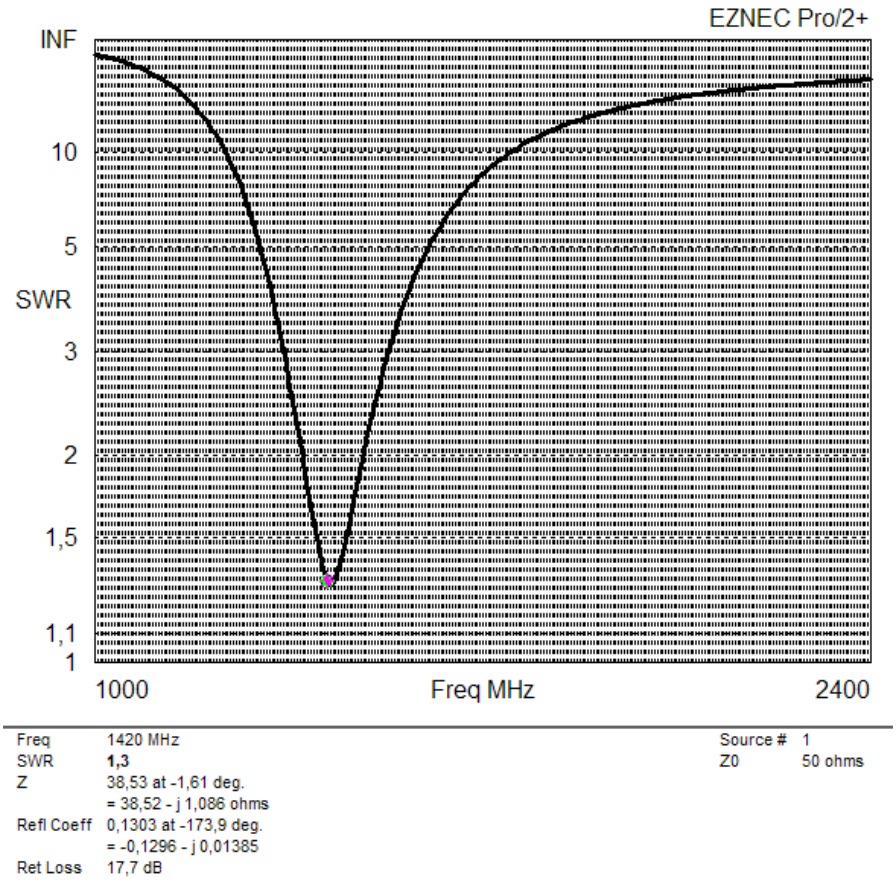

Figure 3.2: Simulated SWR of a slightly shortened half-wave dipole at 1.42 GHz in free space.

3.3.3 Higher-Order Resonances

An ideal dipole supports resonances at odd multiples of the fundamental frequency. In theory,

$$f_n \approx n\, f_1, \quad n = 3, 5, \ldots$$

These modes manifest as additional SWR minima at higher frequencies. As described in Fig. 3.3 these harmonics show for a simulated 1.7 GHz antenna. The antenna adjustments as referenced in Ref. [33] were simulated for a potential execution at a later point.

3.3.4 Three-Dimensional Pattern

The 3D radiation pattern of the 1.42 GHz dipole is shown in Figure 3.4. The toroidal shape is characteristic of an ideal half-wave dipole and a peak gain of approximately 2.4 dBi.

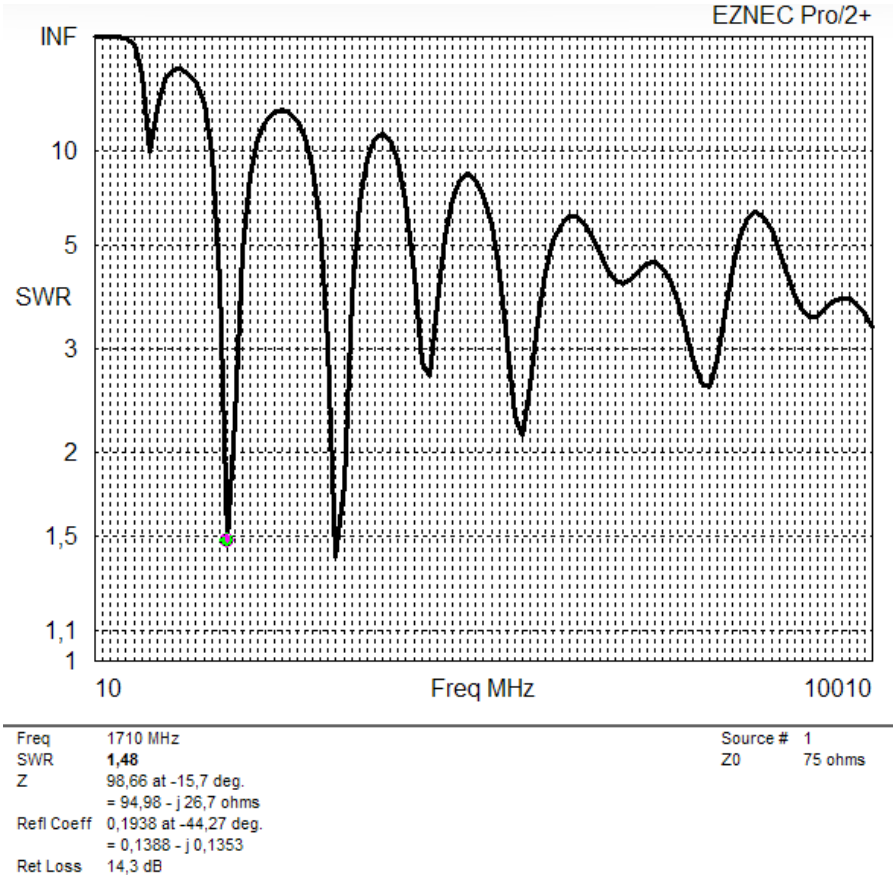

Figure 3.3: Simulated SWR sweep showing harmonics of an ideal half-wave dipole at 1.7 GHz in free space.

3.4 Summary

Numerical simulations using EZNEC Pro/2+ have demonstrated the basic behaviour of a half-wave dipole designed for the hydrogen line at 1.42 GHz. The simulated SWR minimum of 1.30:1 and radiation patterns (2.4 dBi gain, omnidirectional azimuth) confirm theoretical expectations. Higher-order resonances at odd harmonics are inherent to the dipole structure. Practical deviations due to feed hardware and element thickness require further tuning and matching, which are beyond the scope of this theoretical chapter.

3.4.1 Vector Network Analyzer

A Vector Network Analyzer (VNA) is an instrument that measures the complex scattering parameters of an RF network by comparing incident and reflected waves at its ports. In a one-port configuration, the VNA injects a known signal into the antenna feed and records the reflected wave to compute the reflection coefficient S_{11}. In a two-port configuration, forward transmission (S_{21}) and reverse transmission (S_{12}) can also be obtained. In this

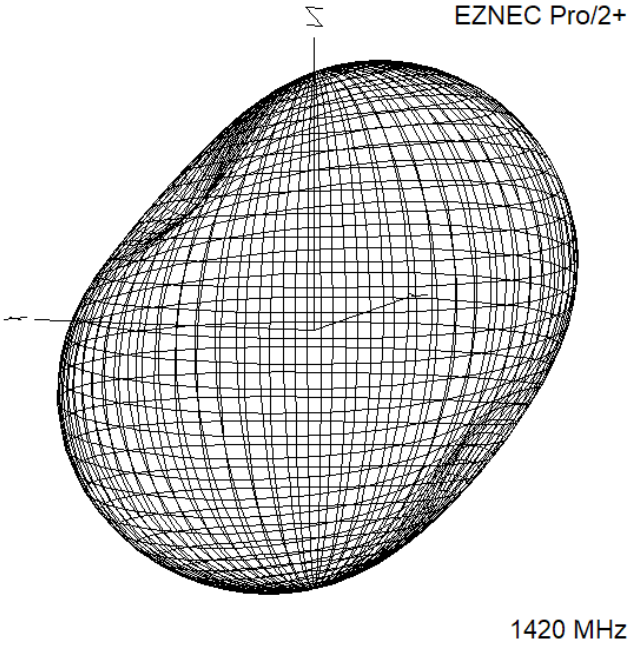

Figure 3.4: Simulated 3D radiation pattern of the dipole at 1.42 GHz in free space.

work, the VNA was used to sweep the frequency band from 1.0 GHz to 3.0 GHz and to record reflection (SWR traces) for the dipole and transmission (coupling) data for the LNA.

3.4.2 S11 parameters

The parameter S_{11} represents the input reflection coefficient of the antenna and is related to the return loss by [34]

$$\mathrm{RL} = -20 \log_{10} |S_{11}| \,.$$

A deep null in S_{11} (large negative dB) corresponds to good matching. Figure 3.7 shows the measured magnitude of S_{11} in dB for the dipole from 1.0 GHz to 3.0 GHz. The return loss at 1.42 GHz is approximately -5.29 dB, indicating that $\approx 28\%$ of the incident power is reflected at that frequency.

Figure 3.8 presents the measured S_{21} magnitude around 1.42 GHz connected to the LNA. A 65 MHz wide peak of approximately (-41 ± 3) dB at 1.420 GHz confirms that the LNA works as expected [40].

3.4.3 Smith Chart

A Smith chart is a normalized polar plot of the complex reflection coefficient, used to visualize the antenna input impedance over frequency. Figure 3.9 shows the measured S_{11} locus on the Smith chart from 1.0 GHz to 3.0 GHz, with a marker at 1.420 GHz. The input impedance at that frequency is approximately $Z_{\mathrm{in}}(1.42\,\mathrm{GHz}) \approx (107 + j\,73.9)\ \Omega$,

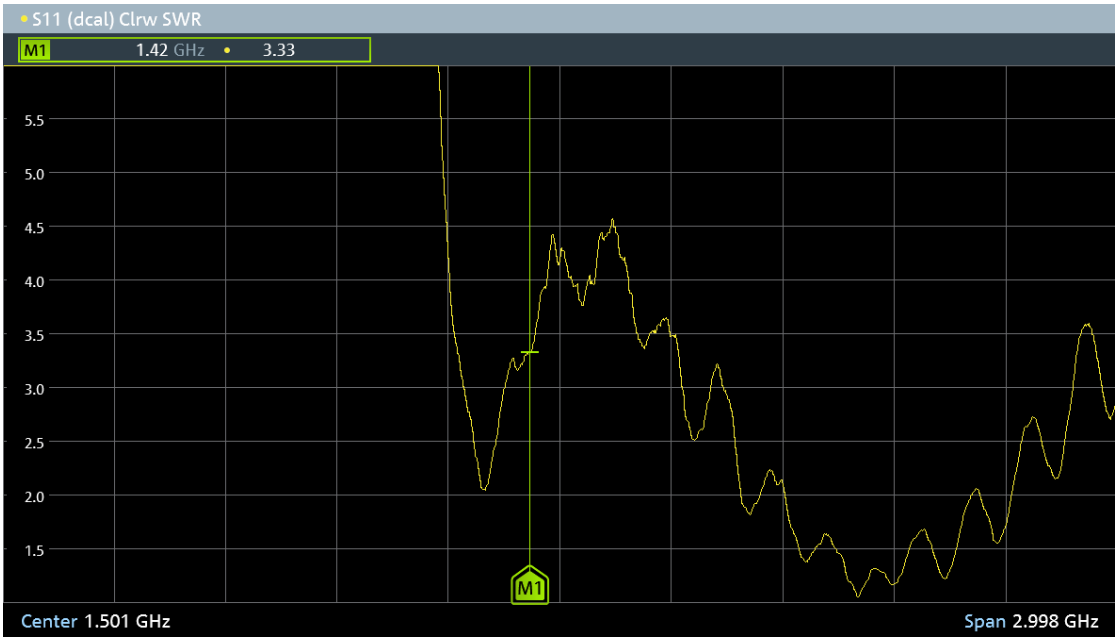

Figure 3.5: Measured SWR versus frequency for the dipole around 1.42 GHz. The marker indicates an SWR of 3.33 at 1.42 GHz.

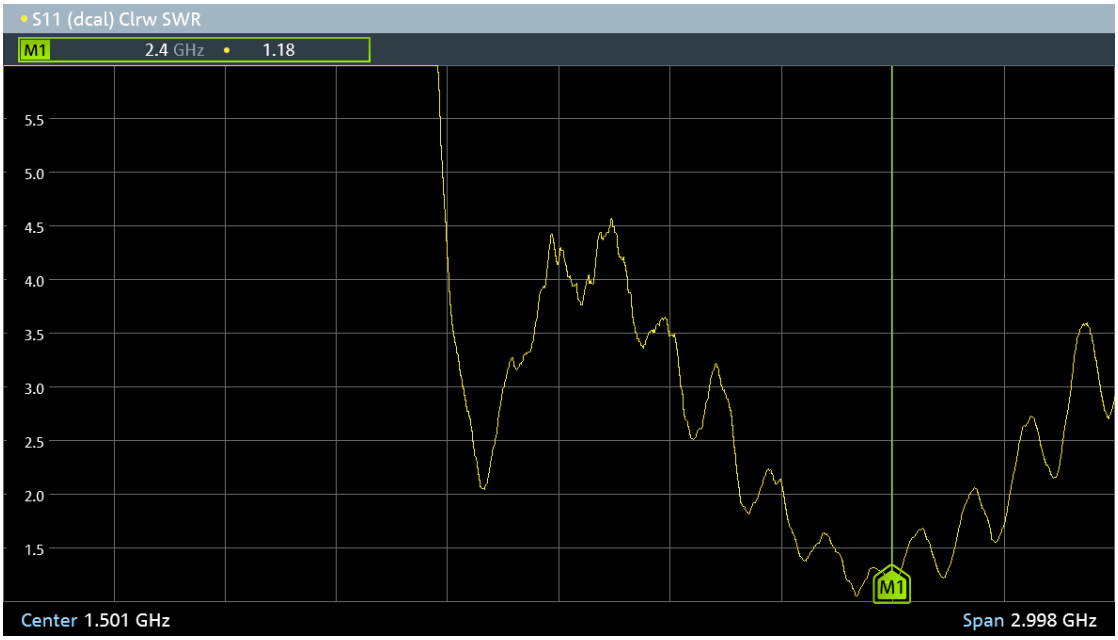

Figure 3.6: Measured SWR of the original 2.4 GHz dipole. The marker indicates an SWR of 1.18 at 2.4 GHz.

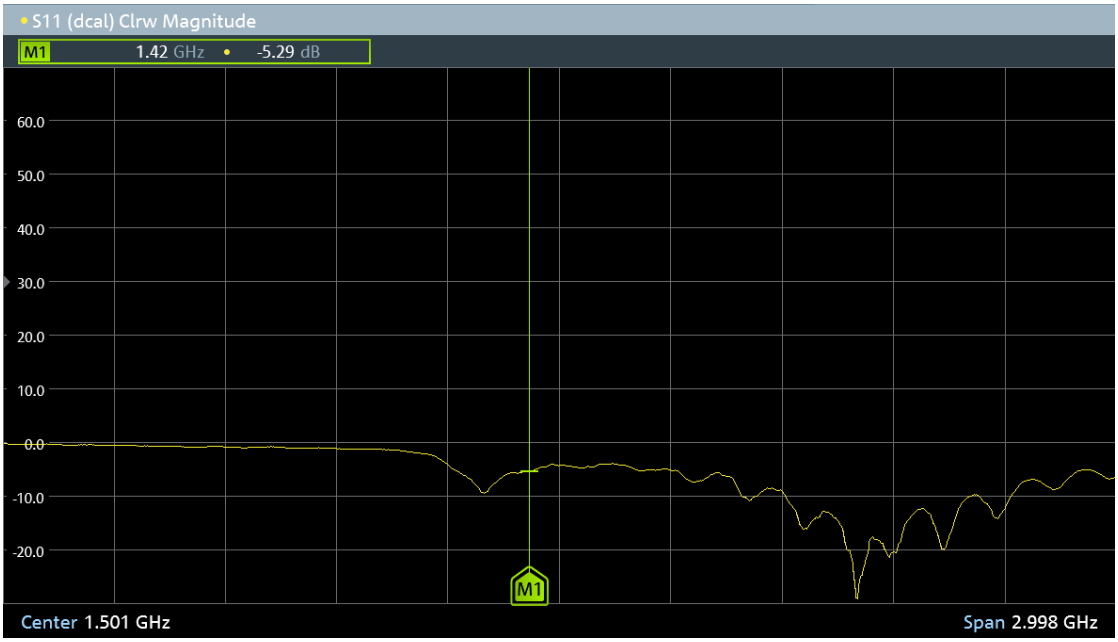

Figure 3.7: Measured S_{11} magnitude (return loss) for the dipole. The marker at 1.42 GHz indicates a return loss of -5.29 dB.

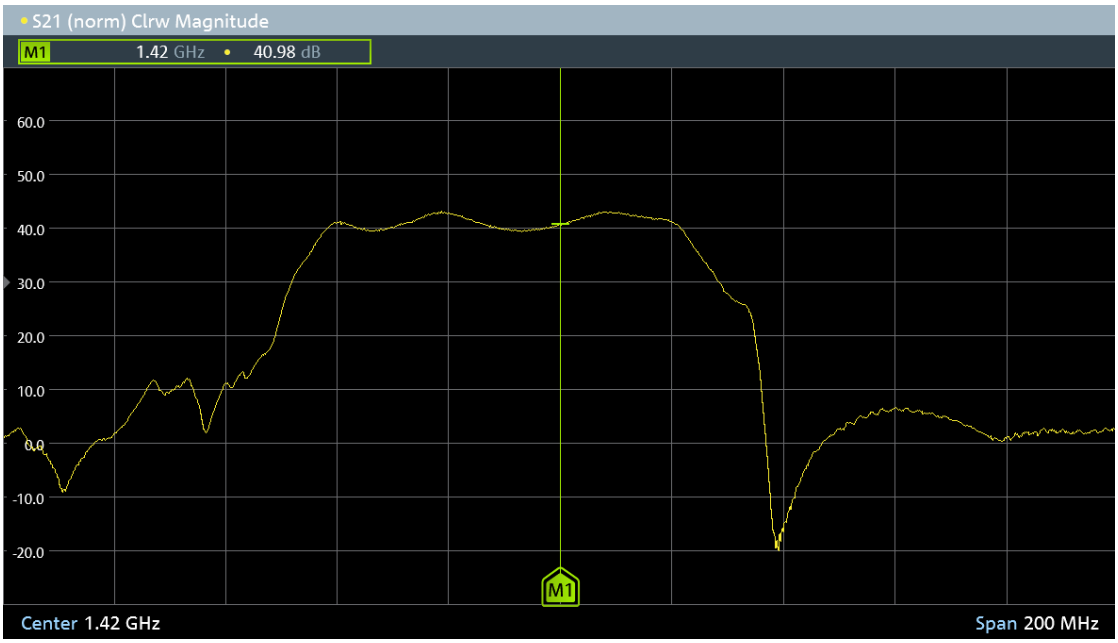

Figure 3.8: Measured S_{21} magnitude for the LNA. The peak coupling of -40.98 dB occurs at 1.420 GHz.

indicating an inductive mismatch and a resistive component more than twice the 50 Ω system impedance.

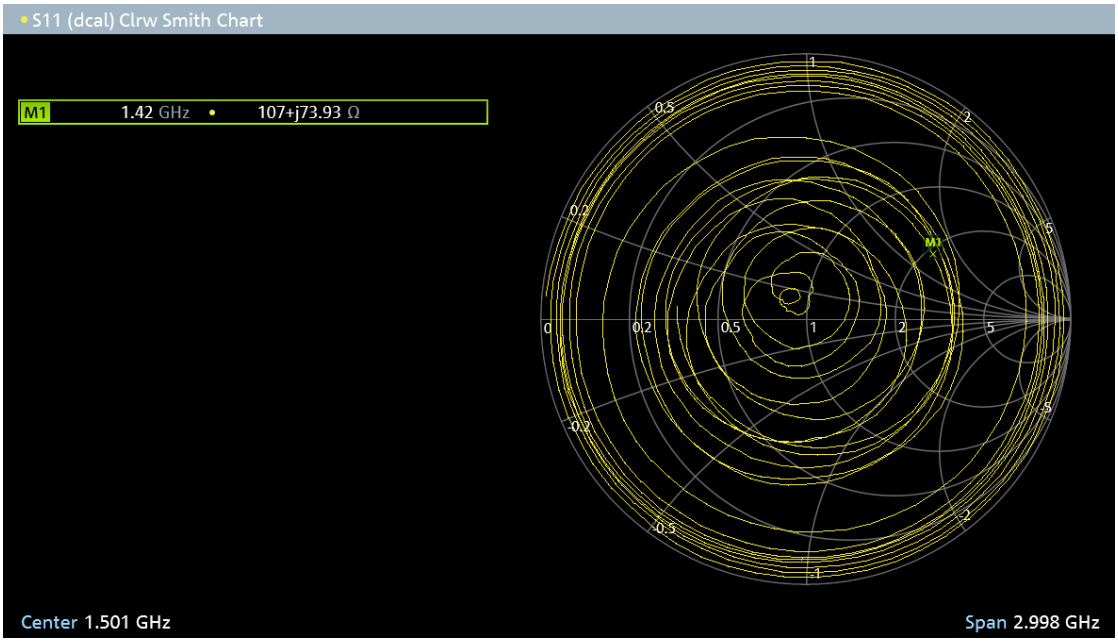

Figure 3.9: Measured S_{11} plotted on a Smith chart. The marker at 1.420 GHz corresponds to $Z_{\text{in}} \approx (107 + j\,73.9)\ \Omega$.

3.4.4 Impedance and Bandwidth

The antenna input impedance Z_{in} and associated standing-wave ratio (SWR) determine the usable bandwidth. Bandwidth is defined as the frequency range over which SWR remains below a specified threshold (e.g. 2:1) or return loss is better than a threshold (e.g. 10 dB). In the present measurements, the dipole exhibits an SWR of 3.33 at the design frequency of 1.42 GHz (Fig. 3.5), and no frequency range around 1.42 GHz fulfills the SWR $\leq$ 2:1 criterion. The limited bandwidth suggests that, for a more robust receive feed, additional element modifications would be required to broaden the SWR $\leq$ 2:1 bandwidth and improve power transfer across the hydrogen line.

4 Receiver Design

This chapter presents the end-to-end design of the hydrogen-line receiver system, encompassing the hardware measurement chain, as depicted in Ref. 4.1, calibrated link-budget analysis, low-noise amplification and filtering, and the software-driven control and data acquisition pipeline to ensure sufficient sensitivity for 21 cm line detection.

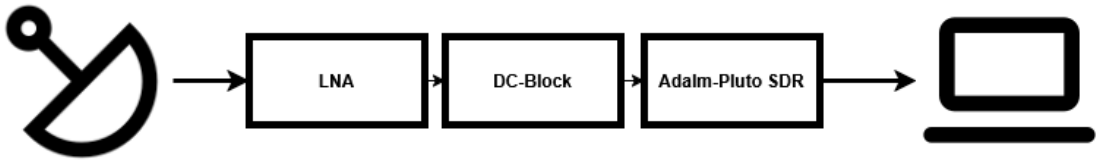

Figure 4.1: Hardware part of the measurement chain

4.1 Link budget

A link budget is a systematic accounting of all power gains and losses that a signal experiences from transmitter to receiver, used to predict the received signal strength and verify that it exceeds the minimum required threshold. This budget guides the choice and configuration of antennas, amplifiers, and cabling to achieve the desired signal-to-noise ratio at the receiver front end. A link budget should be calculated before any measurement endeavors, to determine the scope of any hardware and software adjustments needed for detection.

4.1.1 Antenna

The antenna is a parabolic dish type (60×90cm) with a resonance frequency of 2.4 GHz and a gain of 24 dBi at resonance The antenna feed was analyzed using a VNA, as discussed in Chapter 3. As expected, the Standing Wave Ratio (SWR) is lowest in the 2.4 GHz region, reaching 3.3:1 at the hydrogen line frequency. While SWR values between 1:1 and 2:1 are ideal, a 3.3:1 SWR means that about $20 - 25$ % of the power is lost. The gain G is calculated from Ref. [34] with

$$G = G_0 \cdot \left(\frac{f}{f_0}\right)^2 \tag{4.1}$$

with f as the hydrogen line frequency and f_0 is the antenna resonance frequency of 2.4 GHz, which results in:

$$G_{1.42} = G_{2.4} \times \left(\frac{1.42}{2.4}\right)^2 \approx 24\ \text{dBi} + 10\log_{10}\left(\frac{1.42}{2.4}\right)^2 \approx 24\ \text{dBi} - 5.5\ \text{dB} \approx 18.5\ \text{dBi} \quad (4.2)$$

Thus, we would expect a gain of 18.5 dBi for the mismatched antenna.

4.1.2 System Temperature

Gain and noise temperature are taken from the LNA documentation found in Ref. [40]. The IEEE Standard defines the noise figure as the ratio, of the total noise power per unit bandwidth (at the output frequency) to the portion of that noise which originates from the input source, assuming the source is at the standard noise temperature of 290 K [22]. Tables 4.1, 4.2 and 4.3 showcase the primary calculations needed to estimate the linkbudget.

4.1.2.1 SWR Power Loss

A SWR of 3.3:1 has been measured, due to the frequency mismatch. This causes power to be partially reflected, which reduces the overall power delivered to the system. The power loss can be descibed with [18]:

$$\begin{aligned}\text{Loss (dB)} &= 10\log_{10}\left(\frac{4\cdot\text{SWR}}{(1+\text{SWR})^2}\right)\\ &= 10\log_{10}\left(\frac{4\cdot 3.3}{(1+3.3)^2}\right)\\ &\approx 10\log_{10}(0.714) \approx -1.46\,\text{dB}\end{aligned}$$

Table 4.1: Antenna temperature contributions

Source	**Temperature**
Sky background (Galactic plane)	$50 - 100\,\text{K}$
Atmosphere and ground spillover	$\approx 10 - 30\,\text{K}$
Power loss due to mismatched SWR	-1.46 dB
Assumed total	$\boldsymbol{T_{\text{ant}} \approx 100\,\text{K}}$

Table 4.2: LNA specifications (Nooelec SAWbird+ H1m) [40]

Parameter	**Value**
Center frequency	1420 MHz
Gain	+40 dB
Noise figure	0.8 dB
Noise temperature	$T_{\text{LNA}} = (10^{0.8/10} - 1) \cdot 290 \approx 58.65\,\text{K}$
Bandwidth	65 MHz at 3 dB

Table 4.3: ADALM Pluto SDR characteristics [19]

Parameter	**Value**
Frequency range	325 MHz – 3.8 GHz
Gain (IF/RF/BB)	Up to +73 dB (combined)
Noise figure (typ.)	0.8 dB at G_{max}
Role in chain	Post-LNA; noise contribution negligible due to LNA gain, see also 4.3

The total system temperature thus comes out at:

$$T_{\text{sys}} \approx T_{\text{ant}} + T_{\text{LNA}} \approx 100\,\text{K} + 58.65\,\text{K} = 158.65\,\text{K}\,.$$

4.1.3 Received Power

4.1.3.1 Integrated Flux Density

Flux density in radio astronomy is the power from an emitter that arrives at the telescope's aperture, measured per unit area, per unit frequency interval. It's expressed in Jansky and is defined as:

$$1\ \text{Jy} = 10^{-26}\ \text{W m}^{-2}\ \text{Hz}^{-1}\,.$$

Spectral lines like the Hydrogen line are spread over a small range of frequencies due to Doppler broadening. In this case, the integrated flux density is obtained by integrating the flux density across the entire line profile. This total gives a single number proportional to the overall emission strength, independent of the exact shape, making it easier to compare line sources, with the following relation:

$$S = \frac{S_{\text{int}}}{\overline{v}}$$

Typically strong HI regions in the galactic plane emit $2\,\text{Jy km s}^{-1}$ to $30\,\text{Jy km s}^{-1}$ [45].
For $S_{\text{int}} = 30\,\text{Jy km s}^{-1}$ and $\overline{v} = 30\ \frac{\text{km}}{\text{s}}$, which is typical for a HI cloud, the equation above can be resolved to:

$$S = \frac{30\ \text{Jy} \cdot \text{km/s}}{30\ \text{km/s}} = 1\ \text{Jy}\,.$$

4.1.4 Antenna Effective Area

To describe the effective area of the antenna, the physical aperture area is multiplied with the aperture efficiency. The latter is usually between $0.6 - 0.75$ for parabolic dishes [17] to account for real-world losses that reduce the fraction of power that is actually delivered to the receiver.

- For a parabolic dish:
$$A_{\text{eff}} = \eta \frac{\pi D^2}{4}\,.$$
- with a typical efficiency of $\eta \approx 0.6$ and a diameter of $D = 0.6$ m:
$$A_{\text{eff}} \approx 0.6 \times \frac{\pi \times 0.6^2}{4} \approx 0.17 \text{ m}^2\,.$$

4.1.5 Received Power Calculation

To determine the received power, the velocity needs to be converted into a frequency bandwidth. For this, the Doppler shift relation [20] is necessary, with $f_0 = 1.42$ GHz, a mean rotational velocity [5] of $\Delta v = 200$ km/s, $c = 3 \times 10^5$ km/s:

$$\Delta f = f_0 \cdot \frac{\Delta v}{c} = 947 \text{ kHz}\,.$$

The received power is calculated from the product of flux density and antenna effective area:

$$\begin{aligned} P_{\text{rx}} &= S \times A_{\text{eff}} \\ &= 1 \text{ Jy} \times 0.17 \text{ m}^2 \\ &= 1.7 \times 10^{-27} \text{ W/Hz}\,. \end{aligned}$$

Integrating this spectral power over the computed bandwidth then gives

$$\begin{aligned} P_{\text{rx,total}} &= P_{\text{rx}} \cdot \Delta f \\ &= 1.7 \times 10^{-27} \text{W/Hz} \cdot 947 \text{kHz} \\ &\approx 1.61 \times 10^{-21} \text{ W}\,. \end{aligned}$$

which sets the system's baseline sensitivity requirement and highlights why lengthy integrations and spectral averaging are essential to detect these signals.

4.1.6 System Noise Power

The System Noise Power can be calculated using the bandwidth $B = \Delta v \cdot \frac{f}{c}$, using $\Delta v = 200$ km/s at 1.42 GHz:

$$B = 200 \text{ km/s} \cdot \frac{1.42 \times 10^9 \text{ Hz}}{3 \times 10^5 \text{ km/s}} \approx 947 \text{ kHz}$$

$$\begin{aligned} P_{\text{noise}} &= kT_{\text{sys}}B \\ &= 1.38 \times 10^{-23} \text{ J/K} \cdot 159 \text{ K} \cdot 947 \text{ kHz} \\ &\approx 2.08 \times 10^{-15} \text{ W} = -116.82 \text{ dBm}\,. \end{aligned}$$

4.1.7 Signal-to-Noise Ratio (SNR)

Finally, the SNR can be calculated with the following formula:

$$\text{SNR} = \frac{P_{\text{rx}}}{P_{\text{noise}}} = \frac{1.61 \times 10^{-21}}{2.08 \times 10^{-15}} = 7.74 \times 10^{-7}\,,$$

$$\text{SNR}_{\text{dB}} = 10 \log_{10}(7.74 \times 10^{-7}) \approx -61.11 \text{ dB}$$

.

Interpretation of the Link-Budget Analysis

Component	Value
Antenna gain	18.5 dBi (at 1.42 GHz, 60 cm WiFi dish)
Antenna temperature	100 K (sky + ground)
LNA	40 dB gain, 0.8 dB NF
System temperature	159 K
HI line flux	$2 - 30$ Jy km/s
Effective area	0.17 m^2
Received power	1.61×10^{-21} W
System noise	2.08×10^{-15} W
SNR	-61.1 dB

As shown in Section 4.1, an SNR of -61 dB means the hydrogen-line signal is about 1.3×10^6 times weaker than the instantaneous system noise power. Direct detection in a single spectrum snapshot is therefore impossible, the line will only emerge after substantial integration and averaging.

Using a 4 MHz sampling rate and a 4096-point FFT, the channel width is

$$\Delta f = \frac{f_s}{N} \approx \frac{4 \times 10^6 \text{ Hz}}{4096} \approx 976 \text{ Hz},$$

so each spectral bin spans 976 Hz. Under the radiometer equation [10],

$$\sigma \approx \frac{T_{\mathrm{s}}}{\sqrt{Bt}}$$

with σ as the root-mean-square, T_{s} as the integration time, B for the bandwidth and t as the integration time, it is evident that the RMS noise scales as $1/\sqrt{B\,t}$. For $B = 976$ Hz and $t = 120$ s, the noise-reduction factor is

$$\sqrt{B\,t} \;\approx\; \sqrt{976 \times 120} \;\approx\; 340\,,$$

which corresponds to an SNR improvement of $20\log_{10}(340) \approx 50.6$ dB, lifting the net SNR from -61 dB to about -10 dB.

Hence, the choice of a 120 s dwell time per sky position provides a comfortable margin for pulling the hydrogen-line signal out of the noise. Further filtering as described in the following sections will heighten the signal further.

4.2 Antenna Configuration

To detect and analyze the weak signals of the neutral hydrogen line an optimized antenna system is crucial. The 2.4 GHz WiFi parabolic dish antenna is characterized by its gain (G), beamwidth, and effective collecting area. The antenna gain (G) of a parabolic dish can be theoretically described by the following relationship [1]:

$$G = \eta \left(\frac{\pi D}{\lambda} \right)^2 \tag{4.3}$$

where G is the gain, η is the efficiency factor (typically ranging from 0.5 to 0.7 for practical antennas), D is the diameter of the parabolic reflector, and λ is the observing wavelength. This gain amplifies the inherently weak signals emitted by neutral hydrogen, enhancing the signal-to-noise ratio. The antenna datasheet [49] characterizes G with 24 dBi. The unit dBi stands for a logarithmic measure of an antenna's peak gain compared to an ideal isotropic radiator that emits equally in all directions.

Since the antenna has an elliptical shape, an equivalent diameter needs to be determined using

$$D_{\mathrm{eq}} = \sqrt{a \times b} = \sqrt{60 \text{ cm} \times 90 \text{ cm}} \approx 73.4 \text{ cm} \tag{4.4}$$

This idealization roughly represents a circular aperture with the same collecting area. The beamwidth (θ) of the antenna, crucial for angular resolution, is defined by [1]:

$$\theta \approx \frac{70\lambda}{D} \approx 20.03^\circ \tag{4.5}$$

with θ representing the beamwidth in degrees, λ the wavelength of the observed signal, and D the diameter of the parabolic reflector.

4.3 Amplification and Filtering

Due to the weak nature of the 21 cm signal, amplification and filtering are critical. The chosen component for this function is the Nooelec SAWbird Hydrogen Line Low Noise Amplifier (LNA). This specialized LNA contains a surface acoustic wave (SAW) filter specifically designed for the HI line frequency of 1420 MHz, which reduces out-of-band interference and enhances signal-to-noise ratio (SNR).

The performance of the LNA is characterized by its gain (G_{LNA}) and its noise figure (NF). The overall system noise figure F_{system} considering a cascaded configuration, is approximated by Friis' formula [28]:

$$F_{\mathrm{total}} = F_{\mathrm{LNA}} + \frac{F_{\mathrm{receiver}} - 1}{G_{\mathrm{LNA}}}\,, \tag{4.6}$$

where F_{LNA} and F_{receiver} represent the noise factors of the LNA and the subsequent receiver stage (the ADALM-Pluto), respectively, and G_{LNA} denotes the gain provided by the amplifier. Converting the values from the LNA datasheet [40] from logarithmic to linear scale and inserting them into eq. 4.6 yields the following:

$$F_{\mathrm{total}} = 1.202 + \frac{1.78 - 1}{10^4} = 1.20 + 4.9 \times 10^{-5} \approx 1.2\,. \tag{4.7}$$

Converting back into a noise figure results in:

$$NF_{\mathrm{total}} = 10\log_{10}(F_{total}) = 10\log_{10}(1.2) \approx 0.8\ \mathrm{dB}\,. \tag{4.8}$$

Since the noise figure of the LNA is noted as 0.8 dB, the high gain of the SDR does not influence the overall noise figure, if a high-gain LNA is set before the receiver. This in line with Friis' predictions, that the LNA noise figure dictates the system noise figure, as used in the Linkbudget 4.1.

4.4 ADALM-Pluto SDR

The Analog Devices ADALM Pluto Software-Defined Radio (SDR) is utilized as the backend receiver. It employs direct sampling and digital signal processing to convert the received radio frequency signals into digitized data. The device operates in the frequency range from 325 MHz to 3.8 GHz, making it suitable for observing the HI line at 1420 MHz.

The relationship between sampling frequency f_s and resolution in frequency (Δf) of the Fourier-transformed signal is expressed by:

$$\Delta f = \frac{f_s}{N}, \tag{4.9}$$

where N is the number of sampled points and f_s is the sampling frequency. Achieving sufficient spectral resolution for observing Doppler shifts of the hydrogen line requires selecting an appropriate sampling frequency and integrating the signal over extended time intervals.

4.5 Galactic Coordinator Scheduler

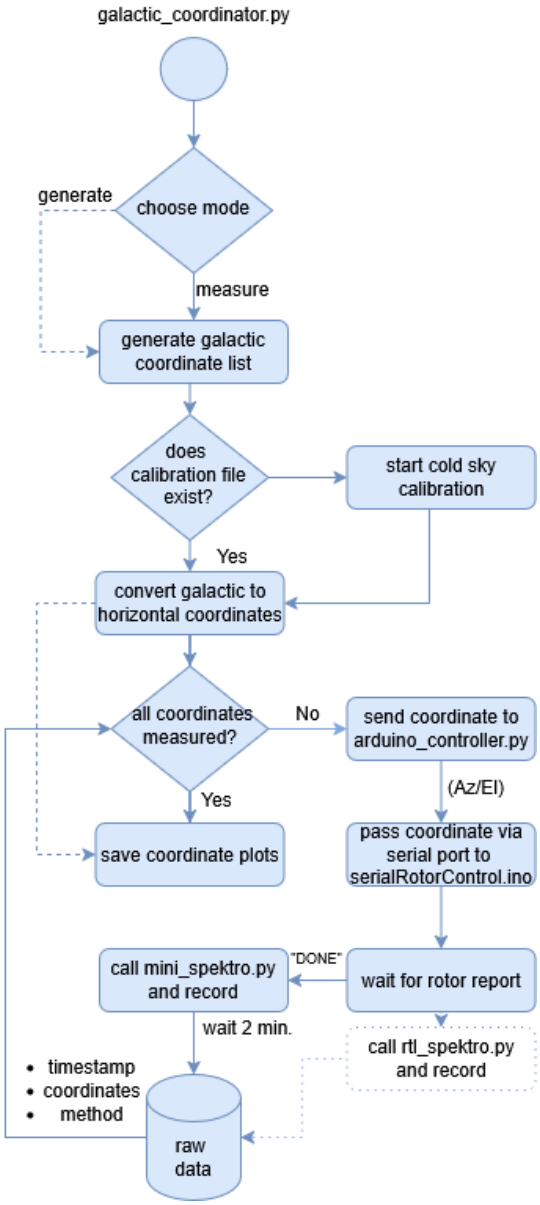

Figure 4.2: Measurement software pipeline

Capturing multiple points along the galactic plane requires an automated measurement pipeline that coordinates the antenna pointing, data acquisition and storage for post-processing. The overall flow is illustrated in Figure 4.2, which provides a block diagram of the software and hardware interaction.

4.5.1 Galactic Coordinate Scheduler

A python script (`galactic_coordinator.py`) computes the desired pointing positions in the galactic plane, with various longitudes in 5-degree steps. The step size can be adjusted using input arguments, as well as the starting point. The script converts Galactic coordinates (ℓ, b) of target points into the local horizontal coordinates (azimuth and elevation) for the observing site and time. This involves transforming Galactic coordinates to equatorial coordinates (Right Ascension and Declination), then to horizontal coordinates using the observer's latitude, longitude and the current sidereal time, in regards to the Earth's continued rotation, using the Python library Astropy [8].

The library ensures accurate pointing for each observation slot. The output is a series of (Azimuth, Elevation) angles that the dish must point to in order to observe the desired Galactic targets. The script also generates plots for both azimuth and elevation, as well as a polar sky plot, for a quick visual sanity check before measuring. Other software tools like Stellarium [44] were used to confirm the accuracy of the pointing coordinates. Per default, the galactic latitude is set to zero, but can also be passed as an optional argument to observe other coordinates.

4.5.2 Antenna Rotor Control

The YAESU G-5500DC Azimuth-Elevation Rotator System [50] was used to steer the antenna to the right position. An unpublished Arduino control script [38] has been altered to integrate it into the existing pipeline. The script `galactic_coordinator.py` communicates with an Arduino microcontroller over serial interface. The altered script `serialRotorControl.ino` interprets the target azimuth/elevation angles and drives the rotor to that position, when it sends the confirmation `"DONE"` to the Python script.

4.5.3 Data Acquisition

When the confirmation signal is received by the Python script, the script `mini_spektro.py` is called. The latter has been built using the libIIO library [9] by AnalogDevices along with GNU Radio, to build a minimal working version of a data acquisition tool. This script was then altered, to fit into the measurement pipeline and collect raw I/Q samples for two minutes using the ADALM Pluto SDR. The script tunes slightly to the larger frequency side of the Hydrogen line frequency and sets the sampling rate to the desired rate (4 MHz) per default. This ensures that the DC spike, that appears at the tuned frequency does not obscure the Hydrogen line. The DC spike is an artifical peak at the center frequency of a spectrum of an SDR, caused by leakage between the in-phase (I) and quadrature (Q) channels during direct sampling, and does not represent a real signal. This data is then stored as binary files containing 32-bit floating point I and Q values.

The filename is tagged with the timestamp and pointing information, for later reference in analysis.

4.5.4 Cold Sky Calibration

Before measuring, a cold-sky measurement is manually performed by pointing the antenna dish to a reference blank sky region with minimal HI emissions, away from the galactic plane. The cold sky data serves as a baseline to calibrate the power spectrum. Since the system does not contain a noise diode or hot load, the cold sky is used as an approximation of the zero signal, to filter out cosmic background and receiver noise. The same integration time will be used, so that noise statistics will be comparable. The cold sky will be subtracted from the on-source spectrum.

4.5.5 Metadata

The `galactic_coordinator.py` script integrates logging functionality, so that timestamps, pointing angles and any status or error messages will be captured during measurement. This allows the system to be kept by itself without having to oversee the process for longer measurements.

4.6 First Light

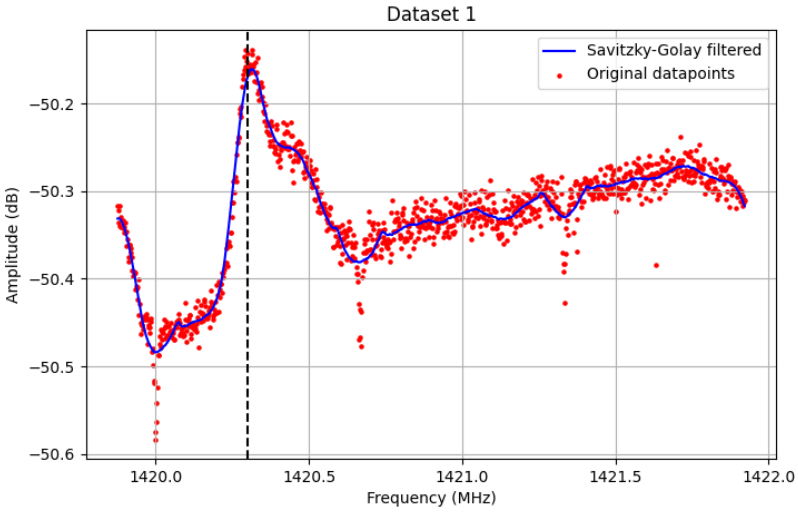

Figure 4.3: First successful measurement of the Hydrogen line

The graph 4.3 shows first successful measurements of the Hydrogen line. The points have been filtered with according to the Savitzky-Golay method [26], to filter out the strong noise and artifacts represented by the red points. The dashed line represents the

rest frequency of the Hydrogen line. Multiple measurements in the same position confirm that this is in case the Hydrogen Line. The power levels lay a little above the estimations calculated in the theoretical linkbudget and confirm these calculations. However, the strong sidelobes and noisy spikes also attest to the necessity of more filtering and data extraction methods in the software pipeline.

5 Doppler-frequency estimation

Digital signal processing (DSP) is fundamental to extracting and interpreting the HI signals received by the antenna system. After the analog-to-digital conversion performed by the ADALM-Pluto SDR, several signal processing steps are essential to reveal the characteristic spectral signature of the hydrogen line. In this project, raw In-Phase and Quadrature (I/Q) data has been collected as is, to be later put through the DSP chain tuned around the HI frequency. Following filtering, the Fast Fourier Transform (FFT) algorithm is applied to translate time-domain samples into frequency-domain spectra. The FFT resolution, directly dependent on the sampling frequency f_s and the number of data points N, determines the system's capability to resolve fine spectral details such as Doppler shifts induced by galactic rotation.

The processing pipeline involves the following steps:

1. Data Acquisition: Raw IQ data is read from binary files, where each complex sample consists of two 32-bit floating-point numbers representing the real and imaginary parts.

2. Windowing: To mitigate spectral leakage, a custom window function is applied to the data. This window is a product of a sinc function and a Hamming window, designed to balance main-lobe width and side-lobe suppression.

3. FFT Computation: The windowed data is passed to the FFT function to compute its frequency spectrum. The FFT output is then shifted using `fftshift` to center the zero-frequency component.

4. Power Spectrum Calculation: The squared magnitude of the FFT output is computed to obtain the power spectrum, which represents the distribution of power across the frequency components.

5. Normalization: The power spectrum is normalized by the total energy of the window function to ensure consistency across different measurements.

5.1 In-phase & Quadrature Data

In DSP, I/Q data refers to the representation of a signal by its two orthogonal components, the in-phase (I) and quadrature (Q) channels. Instead of processing the carrier wave directly, the incoming waveform is mixed down to baseband via multiplication with cosine

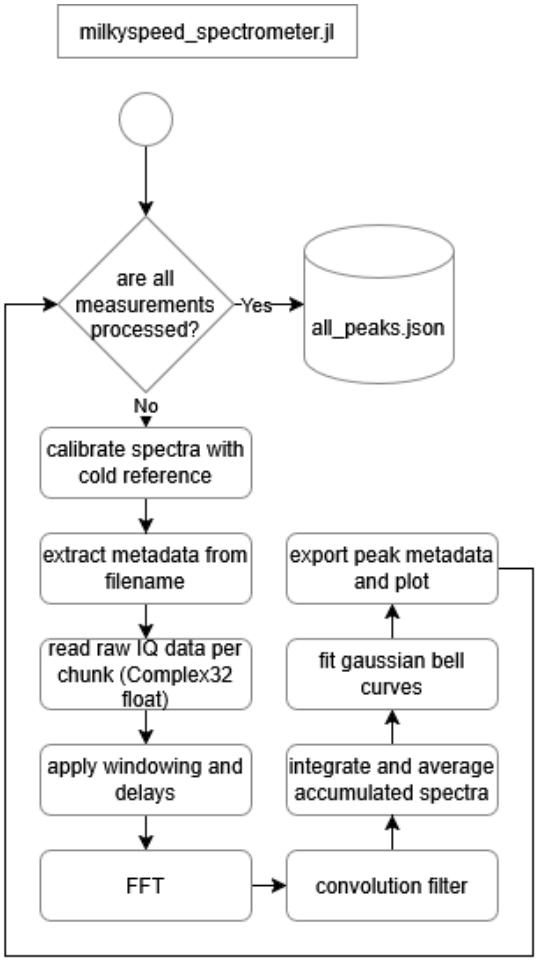

Figure 5.1: Flowchart of the postprocessing Julia script

and sine waves of the carrier frequency. By convention, this results in two real-valued sequences [31]:

$$I[n] = A[n] \cdot \cos(\Phi[n]), \quad Q[n] = A[n] \cdot \sin(\Phi[n])$$

with $A[n]$ and $\Phi[n]$ representing the instanteneous amplitude and phase of the original signal at the n^{th} sample.

Together, each sample pair can be encoded as a complex signal:

$$s[n] = I[n] + j \cdot Q[n] = A[n]e^{j\Phi[n]}$$

The signal traces out a rotating phasor in the complex plane, as shown in 5.2. The information about amplitude and phase is in the I/Q-pair. This simplifies DSP tasks like filtering, (de-)modulation and spectral analysis, by shifting all operations to lower frequencies, without having to handle the original carrier frequency directly.

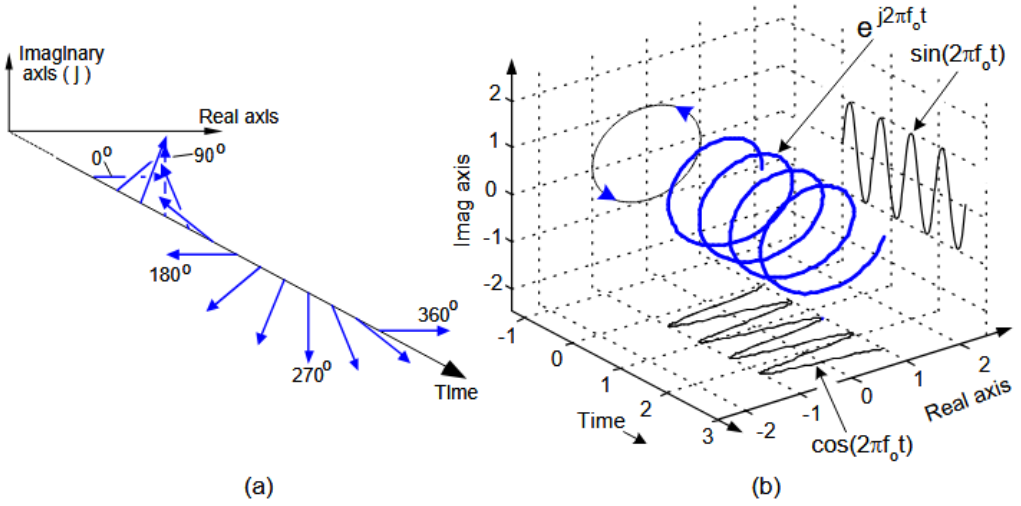

Figure 5.2: (a) shows the real phasor with its 90°-shifted component, (b) shows the same motion as a 3D spiral over time, with projections onto the real axis $I[n]$ and imaginary axis $Q[n]$. Picture adapted from Ref. [31].

5.2 Polyphase Filterbank

To improve spectral resolution and suppress spectral leakage in the measurements, a Polyphase Filterbank (PFB) was implemented as the core of the signal processing pipeline. The PFB serves as a front-end spectral estimator prior to Fourier transformation and is crucial for reducing the influence of side lobes and broadband noise in the power spectrum.

5.2.1 Principle

Standard window FFT approaches suffer from the trade-off between main-lobe width and side-lobe suppression, typically handled with Hann, Hamming, or Blackman windows. However, with strong off-band interference and low signal-to-noise ratio (SNR) signals, windowing alone is insufficient. The PFB addresses this by segmenting the input stream into overlapping blocks, applying windowing functions in parallel to time-delayed versions of the signal, and summing their contributions prior to the FFT [35].

This results in superior channelization and an effective increase in stopband attenuation without degrading the passband response, making Passband Filters ideal for radio astronomical environments with strong off-band interference and low-SNR [21].

5.2.2 Window Construction

A custom-designed prototype filter was used, based on the product of a sinc function and a Hamming window. The sinc function enforces ideal brick-wall low-pass behavior [13] in

the frequency domain, while the Hamming window suppresses side lobes [35].

$$w[n] = \text{sinc}\left(\frac{n}{M}\right) \cdot \text{hamming}(n)\,, \tag{5.1}$$

wih M being the cutoff frequency. These windowed coefficients are reshaped into a matrix of four parallel phases corresponding to the four polyphase filterbank components.

5.2.3 Filterbank Operation

The input stream is processed in overlapping blocks, each of which is filtered by the four polyphase branches and then transformed by an N-point FFT [7]. For each chunk, the four delayed signal segments are multiplied by their corresponding phase of the window matrix. These segments are then recombined and transformed into the frequency domain using the FFT. The resulting power spectrum is normalized by the window energy to ensure spectral consistency:

$$P(f) = \frac{1}{E_w} \cdot |\text{FFT}\{\sum_{i=1}^{4} x_i[n] w_i[n]\}|^2\,, \tag{5.2}$$

where $E_w = \sum |w[n]|^2$ is the energy normalization factor and x_i are the amplitudes at the n^{th} timestep. This design has been adapted from the research program DSPIRA, where a similar filterbank was built in GNURadio [14].

5.2.4 Averaging and Smoothing

To enhance the SNR, we average power spectra over multiple overlapping time chunks. A convolution-based smoothing filter with kernel $[1, 2, 1]/4$ is applied post-FFT to suppress narrowband noise spikes without significantly broadening real spectral features. A kernel is a small matrix using convolution between the kernel and the data to smooth out spikes without broadening true spectral peaks. Every point is spread to itself by 50% and 25% to each immediate neighbour and normalized so that the total power remains unchanged.

5.2.5 Implementation Details

The polyphase filterbank is implemented in Julia using the `DSP.jl` and `FFTW.jl` packages [16]. Efficient chunking of the raw data is handled by low-level binary access and reinterpretation of interleaved IQ samples. The full processing pipeline is defined in the `integrate_file` and `process_windowed_fft` functions. This method was chosen because of its computational efficiency [21].

5.3 Fast-Fourier-Transform

The Fast Fourier Transform (FFT) is a computational algorithm designed to efficiently compute the Discrete Fourier Transform (DFT) of a sequence, or its inverse. The DFT

is a mathematical technique that transforms a sequence of complex numbers in the time domain into another sequence of complex numbers in the frequency domain. This transformation is crucial in signal processing, as it reveals the frequency components present in a time-domain signal. The FFT achieves its efficiency through the Cooley-Tukey algorithm, which recursively splits the DFT into smaller sub-transforms, leveraging symmetry and periodicity in the twiddle factors, as defined by Cooley and Tukey [12]:

$$e^{\frac{-i2\pi kn}{N}} \tag{5.3}$$

Mathematically, the DFT of a sequence $x_0, x_1, \ldots, x_{N-1}$ is defined as [11]:

$$X_k = \frac{1}{N} \sum_{n=0}^{N-1} x_n \cdot e^{i2\pi k \frac{n}{N}}, \quad k = 0, 1, \ldots, N-1 \tag{5.4}$$

Computing the DFT directly from this definition requires $O(N^2)$ operations, which becomes computationally intensive for large N. The FFT reduces this complexity to $O(N \log N)$ by exploiting symmetries and redundancies in the computation, making it feasible to process large datasets efficiently [32].

In the context of the hydrogen line observation, the FFT is employed to transform time-domain I\Q (in-phase and quadrature) data into the frequency domain, enabling the identification and analysis of spectral lines corresponding to hydrogen emissions.

5.3.1 The Cooley-Tukey algorithm

The basic algorithm works as follows: Recursive splitting: If N is even, split DFT into two smaller DFTs: In the radix-2 Cooley–Tukey FFT, each pair of length-$N/2$ sub-transforms $E[k]$ (even) and $O[k]$ (odd) is recombined via the butterfly operation

$$X[k] = E[k] + W_N^k \, O[k], \quad X[k + N/2] = E[k] - W_N^k \, O[k],$$

where $W_N^k = e^{-2\pi i \, k/N}$ are the twiddle factors that adjust the phase of the odd-indexed outputs.

These twiddle factors satisfy the symmetry

$$W_N^{k+N/2} = - W_N^k,$$

so that half of them differ only by a sign, allowing reuse or sign-flip optimizations at each stage.

For an in-place implementation, the input sequence is first permuted by the bit-reversal mapping, which sends each index n (in binary) to its reverse-bit equivalent in $\{0, \ldots, N-1\}$.

This bit-reversal ensures that, at each of the $\log_2 N$ FFT stages, butterflies access data in contiguous memory blocks, minimizing cache misses and data movement.

The total arithmetic effort satisfies the recurrence

$$T(N) = 2\,T(N/2) + O(N),$$

which solves to

$$T(N) = O\big(N \log_2 N\big),$$

a substantial improvement over the $O(N^2)$ operations of a direct DFT.

For example, when $N = 4096$, the FFT requires on the order of

$$4096 \log_2(4096) \approx 4096 \times 12 \approx 4.9 \times 10^4$$

butterfly operations, instead of roughly $4096^2 \approx 1.68 \times 10^7$ multiplies and adds.

These characteristics, reuse of twiddle factors, in-place butterfly recombination, and asymptotic $O(N \log N)$ scaling show the value of the Cooley–Tukey FFT in astronomical spectral analysis.

5.3.2 Implementation Details

The implementation utilizes the FFTW.jl library, a Julia wrapper for the FFTW (Fastest Fourier Transform in the West) C library, known for its efficiency and adaptability to various input sizes [16].

The FFT is integral to various applications in signal processing, including:

- Spectral Analysis: Identifying frequency components within signals, crucial for detecting hydrogen line emissions in radio astronomy.
- Filtering: Designing and applying filters in the frequency domain to isolate or remove specific frequency bands.
- Convolution and Correlation: Efficient computation of convolutions and correlations via the convolution theorem, which states that convolution in the time domain corresponds to multiplication in the frequency domain.
- Data Compression: Transforming signals to the frequency domain can reveal redundancies, aiding in compression algorithms.

5.4 Moving Average

In the spectral processing pipeline, a moving average filter is applied as a post-processing step to smooth the computed power spectrum. This operation serves to suppress high-frequency noise components and enhance the visibility of broad spectral features such as hydrogen line emissions.

5.4.1 Mathematical Definition

The moving average filter is a finite impulse response (FIR) filter that replaces each element in the data sequence with the average of neighboring values. For a one-dimensional sequence $x[n]$, the filtered output $y[n]$ using a symmetric three-point moving average is given by:

$$y[n] = \frac{1}{4}x[n-1] + \frac{1}{2}x[n] + \frac{1}{4}x[n+1] \tag{5.5}$$

This kernel $[1, 2, 1]/4$ preserves the central value while moderately weighing adjacent values. It acts as a low-pass filter, attenuating sharp peaks or narrowband interference without significantly distorting the underlying broad spectral features.

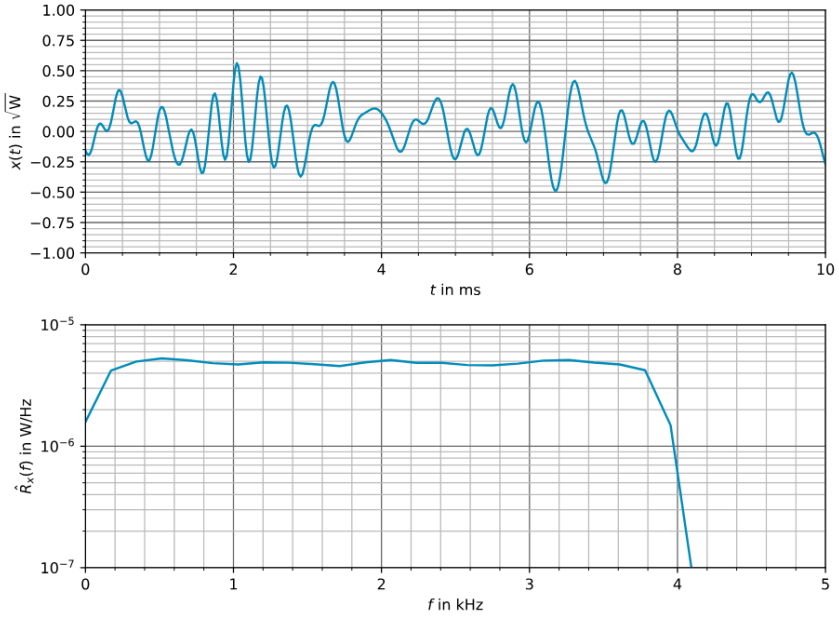

Figure 5.3: Time-domain noise versus Welch-averaged PSD of 4 kHz-band-limited white noise. Adapted from Dietl [13].

Figure 5.3 illustrates the transformation of raw band-limited white Gaussian noise into a smooth spectral baseline via Welch's averaging. In the top panel, a 10 ms snippet of additive white Gaussian noise (AWGN) is shown, each sample is drawn independently from a zero-mean normal distribution, resulting in the characteristic unpredictable "jiggle" around zero. In the bottom panel, the corresponding power spectral density (PSD) estimate is displayed, because white noise has uniform power per hertz, its PSD is flat up to the 4 kHz cutoff and then falls abruptly when the band is limited. This PSD was computed using Welch's method, which splits the record into overlapping, windowed segments, computes periodograms, and averages them to reduce variance in the spectral estimate. Without such averaging, each FFT bin would fluctuate by roughly 6 dB for white noise, obscuring weak spectral lines, the smooth baseline seen here is what enables Doppler-shift detection in these HI measurements.

5.4.2 Application in the Processing Pipeline

In the implemented Julia code, the moving average is applied to the output of the FFT power spectrum, after windowing and normalization. This step is realized using a discrete convolution with the kernel $[1.0, 2.0, 1.0]/4$ and trimming of boundary values:

```
smoothed = conv(spectrum, [1.0, 2.0, 1.0] ./ 4)[2:end-1]
```

.

This operation improves the interpretability of the resulting spectrum, particularly for visual analysis and peak detection, by reducing variance and removing fluctuations. Trimming the convolution output (e.g. `[2:end-1]`) avoids edge artifacts but discards data at the extremes of the spectrum. Mirroring or zero-padding can preserve full length at the cost of minor artifacts.

5.4.3 Performance

The choice of a simple symmetric three-point kernel was motivated by its minimal computational cost and balance between smoothing efficiency and frequency resolution. It was empirically found to reduce unwanted noise in the spectral baseline while preserving the shape and position of hydrogen line peaks. Unlike more aggressive smoothing methods, this approach avoids the risk of merging closely spaced spectral features or artificially broadening narrow signals. The three-point kernel balances noise suppression ($\sim$ 6dB attenuation at Nyquist) and resolution preservation. Larger kernels (e.g. 5-point) provide stronger smoothing but broaden spectral features. The filter's computational efficiency ($O(N)$ complexity) and minimal latency make it ideal for real-time spectral processing, as shown in Ref. [43].

5.5 Results

The graphs 5.4 and 5.5 show how, even with a very weak signal and a mismatched antenna feed, it is possible to extract real cosmic data using modern DSP-techniques. After processing each measurement, the Julia processing pipeline fits Gaussian bell curves to the filtered data and finds its peaks. The peaks are then saved along with the confidence interval parameters and metadata in a `JSON` file, to be later be put through the mapping pipeline.

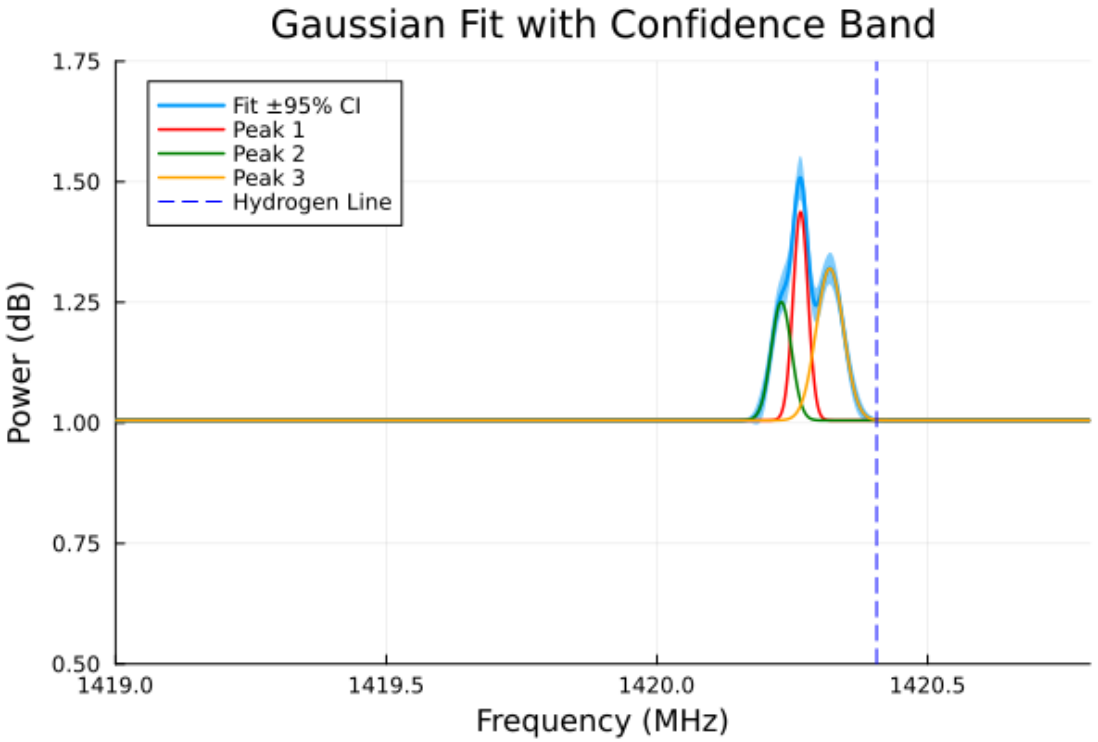

Figure 5.4: Gaussian fit of the periodogramme resulting from the Julia spectrometer pipeline.

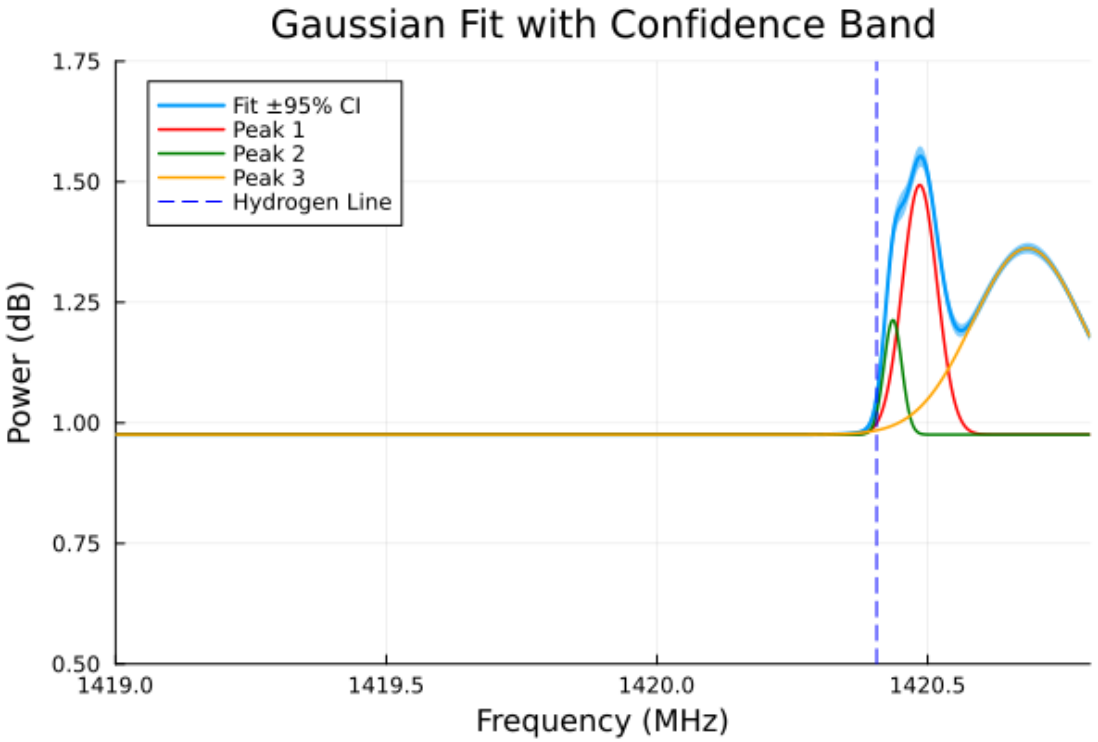

Figure 5.5: Gaussian fit of the periodogramme resulting from the Julia spectrometer pipeline.

6 Mapping the Milky Way

6.1 Galactic Kinematics

Understanding the geometry of the Milky Way requires translating Doppler-derived radial velocities into positions on the galactic plane. While kinematic measurements provide information about the motion of hydrogen clouds, these must be contextualized within a galactic coordinate framework to map the actual structure of the galaxy accurately. This involves converting observed velocities and directions (azimuth, elevation, and time) into galactic positions, followed by triangulation of hydrogen cloud locations within the galactic plane. This mapping offers insights into the distribution and dynamics of matter within the Milky Way.

6.2 Coordinate Systems and Transformations

Accurately mapping the Milky Way necessitates several coordinate transformations. Initially, horizontal coordinates (azimuth and elevation) measured from an observer's position must be converted to equatorial coordinates (right ascension and declination). This step depends on precise information about the observer's geographic location (latitude and longitude) and the exact time of observation (represented as Julian date). Subsequently, equatorial coordinates are transformed into galactic coordinates (longitude l, latitude b), employing a standardized rotation matrix defined by the International Astronomical Union (IAU) [27].

Galactic coordinates specify positions in a reference frame oriented relative to the Milky Way, with galactic longitude l measured counterclockwise from the Galactic Center (GC) and galactic latitude b perpendicular to the galactic plane. Given this project's restriction to observations along the galactic plane ($b = 0°$), the problem simplifies to a two-dimensional projection, significantly streamlining subsequent analysis and visualization.

6.3 Radial Velocity Calculation

Each hydrogen cloud's line-of-sight velocity is determined from the Doppler shift of the 21-cm spectral line. Observed spectral peaks (after calibration and Gaussian fitting of the HI emission profile) yield an observed frequency f_{obs} for the 21 cm line, which is shifted relative to the known rest frequency $f_0 \approx 1420.405$ MHz. The radial (line-of-sight) velocity v_{rad} of the emitting gas is computed using the Doppler formula. For non-relativistic speeds (valid here, as $v \ll c$) applies [4]:

$$v_{\text{rad}} = c \cdot \frac{f_0 - f_{\text{obs}}}{f_0}\,, \tag{6.1}$$

where c is the speed of light. A positive v_{rad} indicates the cloud is receding (redshifted), while a negative value indicates the cloud is approaching (blueshifted). At velocities from tens to a few hundred km/s, the relativistic correction is negligible and the linear formula suffices.

6.3.1 Local Standard of Rest

After determining the raw radial velocity from the frequency shift, a correction is applied to reference this velocity to the Local Standard of Rest (LSR). The LSR is a reference frame in galactic astronomy defined as a point moving in a circular orbit around the Galaxy at the Sun's Galactocentric distance R_0 (with speed V_0). In essence, the LSR represents the mean local rotational motion of stars and gas around the GC. Because the Earth (and Sun) have their own motions relative to this frame, the observed radial velocity is adjusted by the projection of the observer's motion along the line of sight In this work, $V_0 = 220$ km/s and $R_0 = 8.5$ kpc are adopted as the Sun's orbital speed and radius, respectively [37]. The code computes v_{LSR} for each observation and subtracts it from the raw radial velocity. The result is a radial velocity in the LSR frame, which reflects the cloud's motion purely due to Galactic rotation, with the observer's peculiar motion removed. This LSR-corrected velocity is critical for mapping the clouds, since Galactic kinematic models, like the rotation curve, are formulated in the LSR frame.

6.4 Determining Positions of Hydrogen Clouds

Each spectral line of sight contains up to three velocity peaks, indicating several distinct HI clouds at different velocities (and hence different locations) along that line of sight. By determining the central velocity of each Gaussian peak (with typical uncertainties of a few km/s), the analysis obtains a set of radial velocities $v_{\text{rad, i}}$ for potentially multiple clouds i along the same l. These velocities serve as the primary data for subsequent distance calculations. Several methods exist to combine kinematic data with the Milky Way's rotation curve to determine hydrogen cloud positions in the Galactic plane. In this work, two methods are combined to account for different quadrants in the Milky Way.

6.4.1 Tangent Point Method

The tangent point method exploits the highest observed radial velocity in a hydrogen emission spectrum, corresponding to clouds located at the tangent point, where the line of sight is perpendicular to the cloud's orbital radius [4]. The radial velocity at the tangent point, $V_{\texttt{max}}$, allows determination of cloud distance from the GC.

This concept can be demonstrated in Ref. 6.1. The LSR and three hydrogen line clouds are shown in ideal circular orbits around the GC. This idealization is necessary, since the LSR is defined that way. Pointing the telescope along any galactic longitude l with

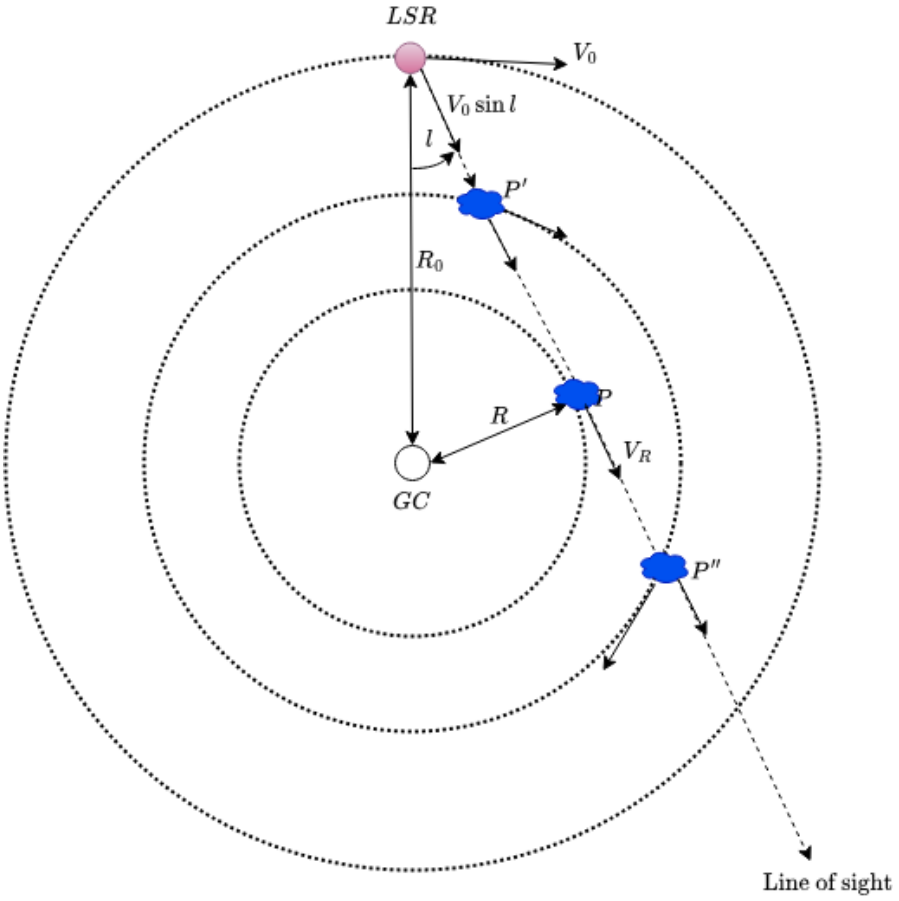

Figure 6.1: Schematic view of the galactic plane from above, with HI clouds at different galactic longitudes l.

$0° \leq l \leq 90°$, since there are no tangent points in quadrant 3 and 4 ($90° \leq l \leq 270°$), results in positive (redshifted) velocites. As shown in the graph 6.1, the Hydrogen clouds P, P' and P" are all along a line of sight, moving in different velocities due to their differing radii R around the GC. The arrows are line-of-sight projections of the velocity. As shown in the figure, only cloud P has a velocity vector purely into the direction of the line-of-sight. Thus, this cloud is moving the fastest away from Earth, meaning the frequency to be measured by this cloud should be redshifted the most (Δf_{min}). In quadrant 4 ($270° \leq l \leq 360°$) this method is possible using the most blueshifted peaks. The radius can be calculated using trigonometry [4]:

$$R = R_0 \cdot \sin l \,, \tag{6.2}$$

where $R_0 = 8.5$ kpc is the Earth's distance from the GC. For $0° \leq l \leq 90°$ (and similarly $R = R_0 |\sin l|$ for Quadrant IV, using the absolute value of $\sin l$).

Combined with the dopplershift formula:

$$V_R = V_{\mathrm{r,\,max}} + V_0 \sin l\,, \tag{6.3}$$

with V_R as the rotational speed of the hydrogen cloud, $V_0 \sin l$ is the LOS projection of the LSR-velocity, which travels with a speed of $V_0 = 220$ km/s in a perfect circle around the GC. v_{LSR} is the LOS projection of the velocity of the observer relative to the LSR. $V_{\mathrm{R(max)}}$ needs to be corrected in the LSR frame as well.

The tangent point method rests on the assumption that hydrogen gas follows roughly circular orbits around the GC. Under this assumption, the largest observed radial velocity indeed corresponds to the tangent point. One limitation is that non-circular motions (e.g. streaming motions in spiral arms or local turbulence) can cause a cloud not at the tangent to exhibit an anomalously high velocity. Additionally, if the HI emission is weak or absent exactly at the tangent location for a given line of sight, the true maximum velocity might not be observed, potentially leading to an underestimated $V(R)$. Despite these caveats, the tangent-point method provides a relatively unambiguous distance for the extremal-velocity cloud and is widely used to trace the inner rotation curve of the Galaxy

6.4.2 Kinematic Distance Method

Since the Tangent Point Method can only supply visual points in the first and fourth quadrant, another method was used to plot points from $90° < l < 270°$, as well as secondary and tertiary peaks in the spectrum. Observed radial velocities are matched to the galactic rotation curve, solving for cloud distances through [4]:

$$V_R = \left(\frac{v(R)}{R} - \frac{V_0}{R_0}\right) R_0 \sin(l), \tag{6.4}$$

The galactic rotation curve plots V_R as a function of radius R to infer distance from velocity. This essentially inverts the radial velocity equation to solve for the galactocentric radius R of the emitting gas. For a known rotation law $V(R)$, the equation can be solved for the radius R that yields the observed v_{LSR} at the given l. In practice, either a flat rotation curve with a profile of $V(R) \approx 220$ km/s, or empirical curves derived from the tangent method may be used, to find the R that satisfies the equation. Once R is determined, the actual physical distance d from the Sun to the cloud can be obtained by geometry. Using the law of cosines in the triangle formed by the Sun, GC, and cloud, one finds:

$$d = R_0 \cos l \pm \sqrt{R^2 - (R_0 \sin l)^2} \tag{6.5}$$

This introduces a fundamental limitation called the near-far-ambiguity in Quadrants I and IV, since every peak returns two possible solutions. The reason for this lies, is that one of these solutions lies between the Sun and the tangent point, with the other one beyond the tangent point on the far side of the galaxy. Without additional information, whether a given radial velocity corresponds to the nearer or farther intersection along

the line of sight cannot be distinguished [46]. In quadrants II and III, the line of sight does not cross the solar circle. Here, $R \geq R_0$, and the distance equation yields a single solution because the discriminant is always positive. In summary, the kinematic distance method allows determining cloud positions for all detected peaks by leveraging a Galactic rotation model, but it requires careful handling of the twofold distance solutions in the inner Galaxy In the code implementation, after obtaining R from the velocity, both d_{near} and d_{far} are computed. Similar to Santo et al. [46], only single positive values would be kept for this work.

6.4.3 Geometric Modeling with Spiral Structure

Incorporating spiral-arm models refines hydrogen cloud positioning by aligning observed velocities with predicted spiral-arm structures. The correlation of observational data to spiral arm models enhances the reliability of positional assignments within the Milky Way's known spiral architecture.

6.5 From Galactic Coordinates to Cartesian Map

Once radial distances have been computed, hydrogen cloud positions can be converted into Cartesian coordinates (x, y) on the galactic plane relative to the Sun's position. Assuming the Sun is located at coordinates $(0, R_0)$, transformations to Cartesian coordinates are:

$$x = -r \sin(l)\,, \tag{6.6}$$

$$y = r \cos(l)\,. \tag{6.7}$$

In this coordinate system, the GC occupies position $(0, R_0)$, with the Sun at $(0, 0)$. This mapping strategy highlights the density and spatial relationships of neutral hydrogen within the Milky Way.

6.6 Gaussian fitting

Given spectral data's inherent noise, Gaussian fitting is essential for accurate velocity extraction, described by:

$$y = \sum_{i=1}^{n} a_i \, e^{-\frac{(x-b_i)^2}{c_i^2}} \tag{6.8}$$

where parameters a_i, b_i, and c_i represent amplitude, central velocity, and peak width, respectively.

These velocities, when mapped via geometric transformations, enable detailed visualization of the Milky Way's spiral structure and dynamics.

6.7 Rotation Curve

The Galactic Rotation curve is a plot, showing the orbital speeds of stars and gas in a galaxy versus their radial distance from the galaxy's center. Collecting the (R, V) pairs from 6.2 and 6.3 enables to infer the rotation speed of the Milky Way as a function of radius from the center. From the assumptions made in the tangent-point method, a flat rotation curve would be expected. Historical astronomical data shows that the rotation curve will rise from $V \approx 0$ near the center to roughly 220 km/s at the solar circle, and remain flat (or only gently decline) beyond R_0. This has been one of the earliest indicators of the presence of dark matter, since experimentally, it continues to stay flat for large R, instead of continuously dropping off as predicted by Kepler's laws.

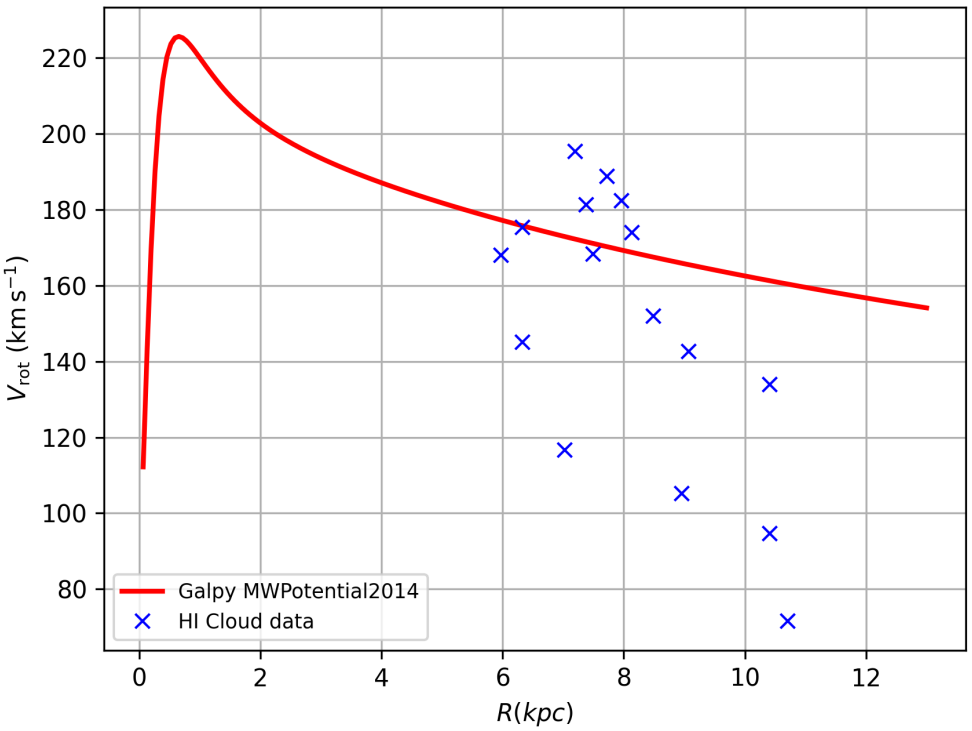

Figure 6.2: Plot showing the experimentally derived rotation curve with a modelled curve by Galpy [3].

While a stronger measurement setup and different filtering techniques may be part of the reason for the large deviation from the model, the Tangent-Point-Method that this derivation relies on, has been found to produce incorrect rotation curves by Chemin et al. [6]. This was found to be caused by an overestimation of velocities in central regions, as well es underestimations around the spiral bar. The tangent-point method only comes

close to the real rotation curve for $4.5 \leq R \leq 8\,\mathrm{kpc}$, which is precisely the reason for the sharp dropoff after 8 kpc in Ref. 6.2.

6.8 Results

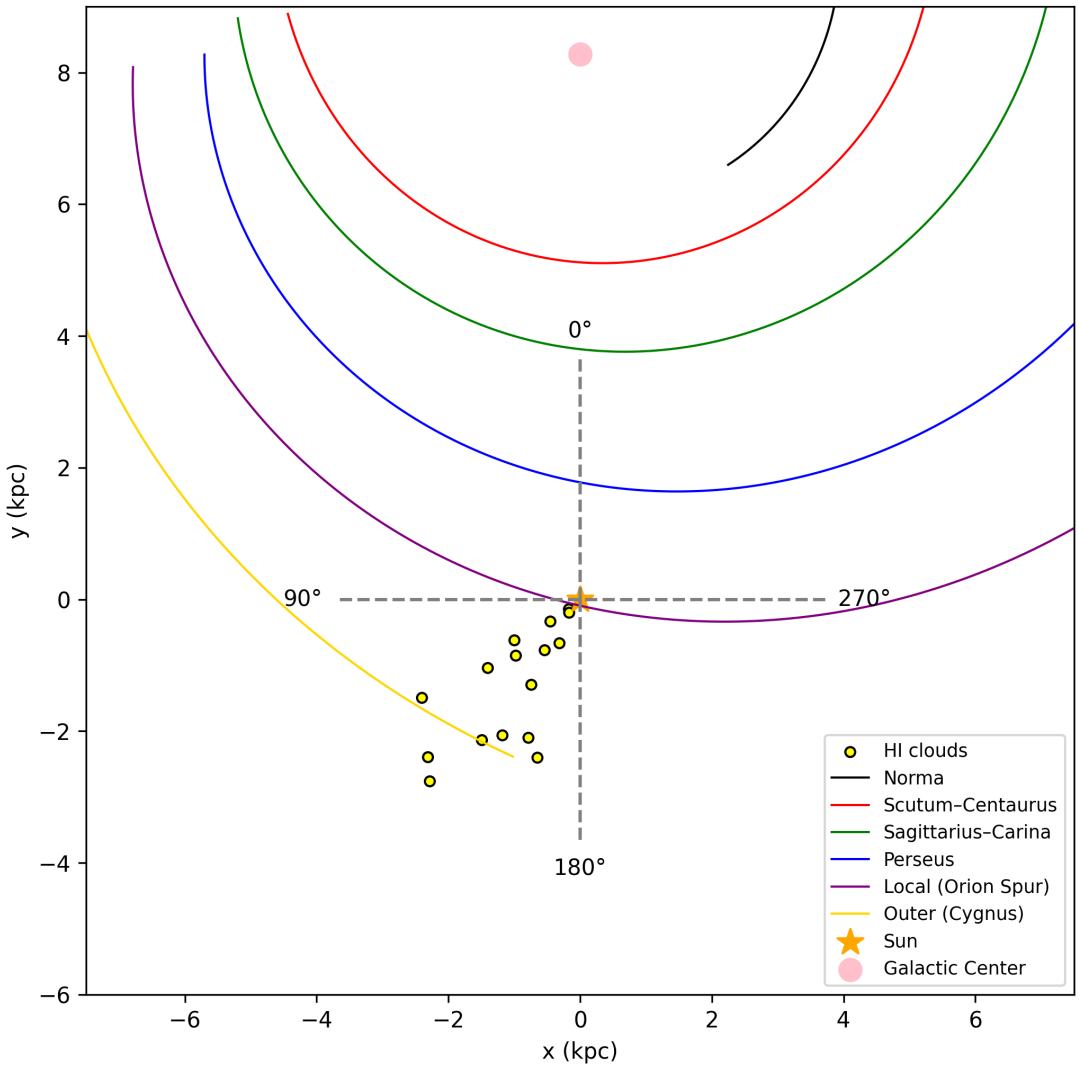

Figure 6.3: Map of the galactic plane, showing a simulated Spiralarm model by Hou and Han

The end result is depicted in Ref. 6.3. Out of 24 measurements, with one to three peaks per longitude, only 16 peaks in total remained, either due to unsolvable ambiguities or unphysical values. A shift of about 1 kpc was needed to align the sun to the Orion

Spur and the Galactic Center at (0, 8.5) kpc and keep these points spaced properly. The arms are drawn using the SpiralMap library for Python [36]. From the library, the model derived by Hou et al. [24] was then used, to plot the spiral structure using a catalog of Galactic HII regions. However, the principle behind plotting multiple overlapping peaks can be seen with some clouds closer to the Outer Arm, and others in the local arm, Orion.

7 Discussion

This chapter interprets the experimental results of this work, to give future continuation attempts an idea of how to improve the results. As evident from the results in 4 and 6, improvements to the system should focus on improving the SNR of the system. Since most of the work of this thesis was done in software, hardware improvements serve as the first obvious solutions, though literature suggests many possibilities to improve the software side of the system as well.

7.1 Hardware improvements

7.1.1 Antenna Feed tuning

Optimizing the feed's impedance match to the 2.4 GHz parabolic dish can reduce reflection losses and boost effective aperture efficiency. Measurements with a vector network analyzer (VNA) showed an $S_{11} \approx -5.29$ dB across the 1420 MHz band, corresponding to $\sim 29.6\%$ power loss. For future work, a tuned dipole or even another feed type could be used to improve SNR.

7.1.2 Parabolic Dish Scaling

Increasing the dish diameter from 0.6 m to 1.2 m doubles the collecting area, yielding a theoretical gain improvement of 6 dB and a beamwidth reduction from $\sim 6°$to $\sim 3°$. However, the narrower beam requires sub-degree pointing accuracy. A mechanical analysis must balance increased gain against structural rigidity and mount precision.

7.1.3 GPS-Disciplined Oscillator

A GPS-disciplined oscillator (GPSDO) combines a high-stability quartz oscillator with the GPS 1 PPS timing signal to minimize both short-term and long-term frequency drift. While the Pluto's native oscillator typically drifts by approximately 1 ppm over several hours ($\approx$ 300 m/s Doppler error at 1.42 GHz) [48], a GPSDO provides a 10 MHz reference with long-term stability better than 0.01 ppm ($\approx$ 3 m/s). Feeding this GPS-referenced clock into the Pluto's CLKIN port effectively eliminates frequency drift, allowing the phase-noise and carrier-offset correction algorithms to operate within a much narrower bandwidth. This simplifies carrier tracking and effectively increases the SNR.

7.1.4 Hot calibration load

Absolute system temperature calibration benefits from the dual-load (Y-factor) method. While the cold-sky reference provides a baseline, adding a hot load (e.g. a matched 50 Ω termination at ambient temperature) yields an accurate temperature scale.

7.2 Software improvements

7.2.1 Advanced Spectral Estimation

Classical FFT resolution is limited by integration time ($\Delta f \approx 1/T$). For unevenly spaced or gapped data, the Lomb–Scargle periodogram [30, 41] retains resolution without interpolation, especially in detecting randomly occuring phenomena, such as pulsars. Subspace methods like ESPRIT [39] and MUSIC [42] exploit eigen-decomposition to resolve closely spaced frequency components beyond the Rayleigh limit.

7.2.2 GUI

A graphical user-interface should also be implemented to improve usability and simplify the measurement process. Most parameters can be set using CLI arguments when running the script. The spectrometer parameters need to be set in its code.

7.3 Limitations

Despite the recommended enhancements, some constraints remain. While an increase in integration time increases the overall power reached to the SDR, extending it beyond 2 minutes would require stable thermal conditions and continuous tracking corrections. Secondly, RFI from the urban observation site close to the ground repeatedly interfered with measurements in lower elevation angles. Mounting the setup to a higher roof or moving the measurement site to a rural area would be expected to record less noise. While a larger dish area would increase the gain, they would also be more prone to wind jitter, so a more stable system with stiffer mounts would be required. Increasing the software complexity demands higher computational load and more careful parameter tuning.

7.4 Future Work

To fully characterize Galactic HI structure, using a specifically tuned dipole and deploying a 1.2 m off-axis dish with GPSDO-stabilized clock and hot/cold calibration for field surveys would be advised for an immediate improvement in SNR. Furthermore, implementing better spectral estimators in Astrojulia and benchmarking against FFT results could be done. During measurement, it may prove beneficial to conduct extended integrations with automatic tracking and active thermal regulation to reach $< 0.1\,\mathrm{K}$ sensitivity. To

extend functionality, developing an automated mapping script over multiple latitudes and automatic calibration pointing would streamline the measurement process.

7.5 Conclusion

In conclusion, the setup proved to reliably record the hydrogen line, with most of the heavy lifting being done in software. This makes it cost-effective, while still enabling to receive the signal in noisy urban environments. There were 25 points recorded along the Galactic latitude 0°. By using an ADALM-Pluto front end, a hydrogen-line specific LNA and a DC-Block, a raw I\Q capture was possible. The Python scripts provide a mostly automatic setup, to combine mapping the measurement route, positioning the Arduino-driven rotor and start the GNURadio flowgraphs for two minutes. During DSP, techniques such as DC offset removal, bandpass filtering, FFT and Multi-Gaussian fitting allowed for an extraction of the hydrogen line, resulting in a JSON catalog of potential HI clouds. Another Python script determines the doppler shift, filters, and then calculates the galactic geometrics to compare the found HI clouds with a model of the Milky Way. Plenty of modification options remain and should foremost aim to improve SNR, to detect the Hydrogen line out of its noisy environment. For future work, many different approaches can be undertaken to extend the set-up. Once a more optimized single setup has been finetuned, it could also easily be replicated and used for radioastronomical interferometry.

Even in urban environments, where light pollution obscures most of the optical realm, this relatively simple and budget-friendly project can be completed to detect the universe's signals in the radiowave domain.

Declaration of Orginality

I hereby declare that the work presented in this thesis is my own and that I have not used any unauthorized sources or assistance. All sources and references used are properly acknowledged and this work has not been submitted elsewhere for any degree or qualification. I further acknowledge that I have used ChatGPT solely for grammar checking, editing, and debugging code, and no other assistance has been provided by the tool in the development of this work.

Gerbrunn, 01.07.2025

References

[1] Constantine A. Balanis. *Antenna Theory: Analysis and Design*. Apr. 4, 2005. ISBN: 978-0471667827.

[2] Rodolfo Cortes Barragan and Andrew N. Meltzoff. "Opportunity to view the starry night sky is linked to human emotion and behavioral interest in astronomy". In: *Nature* (2024). DOI: https://doi.org/10.1038/s41598-024-69920-4.

[3] Jo Bovy. "galpy: A Python Library for Galactic Dynamics". In: *Astrophys. J. Supp* (Dec. 10, 2014). URL: http://github.com/jobovy/galpy (visited on 07/01/2025).

[4] Jed Brody. "Galactic Rotation". Lab theory manual. Emory Education.

[5] Tia Camarillo, Pauline Dredger, and Bharat Ratra. "Median Statistics Estimate of the Galactic Rotational Velocity". In: *MNRAS* (Apr. 5, 2018). DOI: https://doi.org/10.48550/arXiv.1805.01917.

[6] Laurent Chemin, Florent Renaud, and Caroline Soubiran. "Incorrect rotation curve of the Milky Way". In: *Astronomy & Astrophysics* (Apr. 2, 2015). DOI: 10.1051/0004-6361/201526040.

[7] Ayanth Chennamangalam. "The Polyphase Filter Bank Technique". In: *CASPER* (Aug. 6, 2011).

[8] Astropy Collaboration. *Astropy: A community Python library for astronomy*. Version 5.3.4. URL: https://docs.astropy.org/en/stable/ (visited on 06/22/2025).

[9] Astropy Collaboration. *libIIO: Documentation*. Version v0.25. URL: https://libiio.github.io/libiio/v0.25/index.html (visited on 06/22/2025).

[10] James J. Condon and Scott M. Ransom. *Essential Radio Astronomy*. Princeton University Press, Apr. 5, 2016. ISBN: 9780691137797.

[11] Bill Connelly. *Visualizing how FFTs work*. May 29, 2015. URL: https://www.billconnelly.net/?p=276 (visited on 06/25/2025).

[12] James W. Cooley and John W. Tukey. "An algorithm for the machine calculation of complex Fourier series". In: *Mathematics of Computation* 19.90 (1965), pp. 297–301.

[13] Guido Dietl. *Telecommuncation Systems*. Lecture Notes, Julius-Maximilians-Universität Würzburg. 2025.

[14] *Digital Signal Processsing using GNURadio - Fourier Analysis and Radio Astronomy*. Aug. 14, 2020. URL: https://wvurail.org//dspira-lessons/dsplab-fourier2/#57-spectral-leakage--polyphase-filter-bank-pfb.

[15] H.I. Ewen and E. M. Purcell. "Observation of a Line in the Galactic Radio Spectrum: Radiation from Galactic Hydrogen at 1,420 Mc./sec." In: *Nature* (Sept. 1, 1951).

[16] *FFTW Julia Documentation*. May 2017. URL: https://juliamath.github.io/FFTW.jl/stable/.

[17] Charles E. Free and Colin S. Aitchison. *RF and Microwave Circuit Design Theory and Applications*. Wiley, Sept. 3, 2021. ISBN: 9781119114666.

[18] *Fundamentals of RF and Microwave Noise Figure Measurements*. Jan. 10, 2019.

[19] Robin Getz. *ADALM-PLUTO Receiver Sensitivity*. June 22, 2018.

[20] David Halliday, Jearl Walker, and Robert Resnick. *Fundamentals Of Physics Extended*. John Wiley & Sons, Aug. 13, 2013.

[21] Christopher Harris and Karen Haines. "A Mathematical Review of Polyphase Filterbank Implementations for Radio Astronomy". In: *Publications of the Astronomical Society of Australia* (Oct. 19, 2011).

[22] H. A. HAUS, ed. *IRE Standards on Electron Tubes: Definitions of Terms, 1957*.

[23] Helmut Hellwig, Robert F.C. Vessot, Martin W. Levine, Paul W. Zitzewitz, David W. Allan, and David J. Glaze. "Measurement of the Unperturbed Hydrogen Hyperfine Transition Frequency". In: *IEEE Transactions on Instrumentation and Measurement* (Nov. 4, 1970). URL: https://tf.nist.gov/general/pdf/13.pdf (visited on 04/10/2025).

[24] L. G. Hou and J. L. Han. "The observed spiral structure of the Milky Way". In: *Astronomy & Astrophysics* (Oct. 3, 2014). DOI: https://doi.org/10.1051/0004-6361/201424039.

[25] *Hydrogen Line*. Jan. 18, 2009. URL: https://commons.wikimedia.org/wiki/File:Hydrogen-SpinFlip.svg#globalusage.

[26] Inacquaroli. *Implementation of the 1D Savitzky-Golay filter in JuliaLang*. May 2021. URL: https://www.juliapackages.com/p/savitzkygolay.

[27] George H. Kaplan. "The IAU Resolutions on Astronomical Reference Systems, Time Scales, and Earth Rotation Models Explanation and Implementation". In: *UNITED STATES NAVAL OBSERVATORY* (Oct. 20, 2005).

[28] John D Kraus and Ronald J Marhefka. *Antennas*. Tata McGraw-Hill, 1950.

[29] Roy W. Lewallen. *EZNEC Pro/2+ Antenna Modeling Software*. 2004. URL: https://eznec.com/misc/EZNEC_Printable_Manual/7.0/EZW70_User_Manual_A4.pdf.

[30] N. R. Lomb. "Least-squares frequency analysis of unequally spaced data". In: *Astrophysics and Space Science* 39 (1976).

[31] Richard Lyons. *Quadrature Signals: Complex, But Not Complicated*. IEEE. Nov. 2008. URL: https://www.ieee.li/pdf/essay/quadrature_signals.pdf (visited on 06/06/2025).

[32] Steven G. Johnson Matteo Frigo. "The Design and Implementation of FFTW3". In: *Proc. IEEE* (Feb. 2, 2005).

[33] António Pereira. *Optimizing a WIFI Grid Antenna for Maximum Efficiency*. 2023. URL: https://usradioguy.com/optimizing-wifi-grid/ (visited on 06/28/2025).

[34] David M. Pozar. *Microwave Engineering*. Wiley, Nov. 2011. Chap. 14. ISBN: 978-0-470-63155-3.

[35] Danny C. Price. *Spectrometers and Polyphase Filterbanks in Radio Astronomy*. Department of Astronomy, University of California Berkeley, May 10, 2018. DOI: https://doi.org/10.48550/arXiv.1607.03579.

[36] Abhay Kumar Prusty and Shourya Khanna. "SpiralMap: A Python library of the Milky Way's spiral arms". In: *Journal of Open Source Software* (June 13, 2025).

[37] M. J. Reid, K. M. Menten, A. Brunthaler, X. W. Zheng, T. M. Dame, Y. Xu, Y. Wu, B. Zhang, A. Sanna, M. Sato, K. Hachisuka, Y. K. Choi, K. Immer, L. Moscadelli, K. L. J. Rygl, and A. Bartkiewicz. "Trigonometric Parallaxes of High Mass Star Forming Regions: The Structure and Kinematics of the Milky Way". In: *The Astrophysical Journal* 783.2 (Feb. 2014), p. 130. ISSN: 1538-4357. DOI: 10.1088/0004-637x/783/2/130. URL: http://dx.doi.org/10.1088/0004-637X/783/2/130.

[38] Maximilian Reigl. "Arduino Control Software". Chair of Satellite Communication and Radar Systems, 2025.

[39] Richard Roy and Thomas Kailath. "ESPRIT-Estimation of Signal Parameters Via Rotational Invariance Techniques". In: *IEEE Transactions on Acoustics, Speech, and Signal Processing* 37 (Aug. 6, 1989). DOI: 10.1109/29.32276.

[40] *SAWbird+ H1m Low Noise Amplifier (LNA)*. Dec. 10, 2019.

[41] J. D. Scargle. "Studies in astronomical time series analysis. II. Statistical aspects of spectral analysis of unevenly spaced data". In: *Astrophysical Journal* 263 (1982).

[42] Ralph O. Schmidt. "Multiple Emitter Location and Signal Parameter Estimation". In: *IEEE Transactions on Antennas and Propagation* 34 (Mar. 31, 1986). DOI: 10.1109.

[43] Steven W. Smith. *Digital Signal Processing: A Practical Guide for Engineers and Scientists*. Newnes, 2003.

[44] Stellarium contributors. *Stellarium v25.2 Astronomy Software*. 2025. DOI: 10.5281/zenodo.15715458. URL: https://stellarium.org/.

[45] Nadia Steyn, Renée C. Kraan-Korteweg, Sambatriniaina H. A. Rajohnson1, Sushma Kurapati, Hao Chen, Bradley Frank, Paolo Serra, Lister Staveley-Smith, Fernando Camilo, and Sharmila Goedhart. *Hi Galaxy Signatures in the SARAO MeerKAT Galactic Plane Survey – I. Probing the richness of the Great Attractor Wall across the inner Zone of Avoidance*. Research Report. Department of Astronomy, University of Cape Town, June 12, 2023. URL: https://arxiv.org/html/2312.03545v1 (visited on 06/11/2025).

[46] Syed Ashraf Uddin Tarif Rashid Santo. "Mapping the Spiral Structure of the Milky Way Galaxy at 21cm Wavelength Using the SALSA Radio Telescope of Onsala Space Observatory". In: *International Journal of Astronomy* (2013). DOI: 10.5923/j.astronomy.20130203.03.

[47] W. L. Wiese and J. R. Fuhr. "Accurate Atomic Transition Probabilities for Hydrogen, Helium, and Lithium". In: *Journal of Physical and Chemical Reference Data* (June 24, 2009). DOI: https://doi.org/10.1063/1.3077727.

[48] Analog Devices Wiki. *ADALM-PLUTO Phase Noise and Frequency Accuracy*. June 10, 2019. URL: https://wiki.analog.com/university/tools/pluto/users/phase_noise?s[]=drift.

[49] WiMo. *Datasheet 2.4 - 2.5 GHz Grid Antenna*. URL: https://www.wimo.com/media/akeneo_connector/media_files/1/8/18686.24_c044.pdf (visited on 06/20/2025).

[50] YAESU. *G-5500DC Instruction Manual*. URL: https://static.dxengineering.com/global/images/instructions/ysu-g-5500dc_xb.pdf (visited on 06/22/2025).